



NTNU – Trondheim
Norwegian University of
Science and Technology

Pressure pulsations and stress in a high head Francis model turbine

Julie Marie Hovland

Master of Science in Mechanical Engineering

Submission date: June 2013

Supervisor: Torbjørn Kristian Nielsen, EPT

Norwegian University of Science and Technology
Department of Energy and Process Engineering

EPT-M-2013-55

MASTER THESIS

For
Stud.tech Julie Marie Hovland

Spring 2013

Pressure pulsations and stress in a high head Francis model turbine

Trykkpulsasjoner i modell av høytrykks Francisturbin

Background

In a hydro power plant, the turbines, due to the variation of the electric demand, will be running in different modes of operation outside the design performance point. Hence, the pressure pulsation amplitudes will vary and might give causes to fatigue.

A model of a high head Francis turbine will be installed in the Waterpower Laboratory at NTNU. The model is geometrical similar to an existing prototype turbine installed in a Norwegian power plant. The model is equipped with pressure transducers and strain gauges on one of the runner blades. For different performance, the pressure pulsations in the runner and draft tube shall be measured, as well as the stress on the runner blade.

The Master project shall be done in collaboration with Stud. tech Ingeborg Lassen Bue

Objective

Establish relations between pressure pulsations and stress in the model turbine.

The following tasks are to be considered

- 1 The candidate shall participate in the installing the model turbine in the test rig and setting up the data acquisition system.
- 2 Learn how to run the laboratory
- 3 For different performances, map the pressure pulsation as well as the stress on the runner blades.
- 4 Analyze the pressure pulsations and stresses for components caused by rotor-stator interaction (RSI), draft-tube vortex, and stochastic detachments.
- 5 Check for correlation between the pressure pulsation in the draft tube cone and in the runner channels.

Within 14 days of receiving the written text on the master thesis, the candidate shall submit a research plan for his project to the department.

When the thesis is evaluated, emphasis is put on processing of the results, and that they are presented in tabular and/or graphic form in a clear manner, and that they are analyzed carefully. The thesis should be formulated as a research report with summary both in English and Norwegian, conclusion, literature references, table of contents etc. During the preparation of the text, the candidate should make an effort to produce a well-structured and easily readable report. In order to ease the evaluation of the thesis, it is important that the cross-references are correct. In the making of the report, strong emphasis should be placed on both a thorough discussion of the results and an orderly presentation.

The candidate is requested to initiate and keep close contact with his/her academic supervisor(s) throughout the working period. The candidate must follow the rules and regulations of NTNU as well as passive directions given by the Department of Energy and Process Engineering.

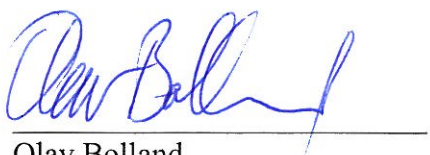
Risk assessment of the candidate's work shall be carried out according to the department's procedures. The risk assessment must be documented and included as part of the final report. Events related to the candidate's work adversely affecting the health, safety or security, must be documented and included as part of the final report.

Pursuant to "Regulations concerning the supplementary provisions to the technology study program/Master of Science" at NTNU §20, the Department reserves the permission to utilize all the results and data for teaching and research purposes as well as in future publications.

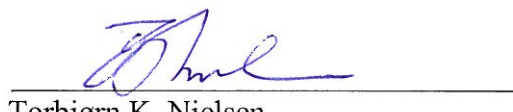
The final report is to be submitted digitally in DAIM. An executive summary of the thesis including title, student's name, supervisor's name, year, department name, and NTNU's logo and name, shall be submitted to the department as a separate pdf file. Based on an agreement with the supervisor, the final report and other material and documents may be given to the supervisor in digital format.

- Work to be done in lab (Water power lab, Fluids engineering lab, Thermal engineering lab)
 Field work

Department of Energy and Process Engineering, 14.January 2013



Olav Bolland
Department Head



Torbjørn K. Nielsen
Academic Supervisor

ACKNOWLEDGEMENTS

This Master thesis is conducted in collaboration with the Waterpower laboratory at the Norwegian university of science and technology (NTNU). Planning and execution of the experiment was performed with fellow student Ingeborg Lassen Bue.

Thanks to professor Michel Cervantes from Luleå university of technology (LTU) for good advice and reassurance during troubled times. Also a great thanks to Kaveh Amiri and Chirag Trivedi for sharing their MATLAB scripts for data analysis.

The guys in the lab; Joar Grilstad, Halvor Haukevik, Trygve Opland and Bård Brandåstrø did a great job on the testrig. Also a great thanks to Stein Kristian Skånøy for helping out with Labview and compact RIO.

Thanks to supervisor professor Torbjørn K. Nielsen for good advice and interesting conversations. I am also very grateful to Phd candidates Bjørn W. Solemslie and Peter Joachim Gogstad for all the time they set aside for this project.

Finally, thanks to Sindre for all the little things that make life enjoyable.



Julie Marie Hovland

Trondheim 10.06.2013

ABSTRACT

Model tests on a high head francis turbine has been conducted at the Waterpower laboratory at NTNU. Simultaneous measurements of the pressure were performed on different parts of the waterway . Compact RIO hardware and Labview software from National Instruments was used for data aquisition.

Pressure sensors were placed at the inlet, vaneless space, runner channel, draft tube cone and draft tube outlet in the rig. Generator torque and the rotational speed of the runner was also measured. Spectral analysis was performed on all measurements to map out frequencies and corresponding amplitues at various load conditions.

The RSI induced pulsations dominates the vaneless space and runner channels. Pressure pulsations are dampened across the runner and sensors at the trailing edge display values that are significantly larger than sensors positioned at the outlet. RSI pulsations are dependent on the flow and relative amplitudes in the vaneless space is reduced with over 90% when the load is lowered from 100% to 50%.

Vortex rope frequency is detected in the runner channels and the generator torque. This suggests that the low frequency oscillations causes a mass oscillation through the system that affects the output of the generator.

An air leakage through the shaft was detected during testing. The incoming air resulted in an excessive draft tube vortex, thus the results obtained in this work are not directly comparable to field test conditions.

Modellforsøk på en høytrykks Francis turbin har blitt utført ved Vannkraftlaboratoriet på NTNU. Simultan prøvetaking på flere kanaler ble utført med compact RIO maskinvare og LabVIEW programvare fra National Instruments.

Trykksensorer ble plassert ved innløpet, omdreiningshulrommet, i roterende kanaler, sugerørskonus og i utløper av sugerøret. Dreiemomentet på generatoren og omdreiningshastigheten til hjulet ble også målt. Spektralanalyse ble utført på alle målinger for å kartlegge frekvenser og tilsvarende amplituder ved ulike driftspunkt.

RSI-induserte pulsasjoner dominerer omdreiningshulrommet og de roterende kanalene. Trykkpulsasjonene dempes gjennom løpehjulet og sensorer ved omdreiningshulrommet viser verdier som er betydelig større enn sensorer plassert ved utløpet av hjulet. RSI pulsasjoner varierer med lasten og synker over 90% ved en lastendring fra 100% til 50%.

Sugerørsfrekvensen er oppdaget i roterende kanaler og i dreiemomentet på generatoren. Dette tyder på at de lavfrekvente svingningene fører til en massevingning gjennom systemet som påvirker generatoreffekten.

En luftlekkasje gjennom akslingen ble oppdaget i løpet av forsøkene. Lekkasjen ble forsøkt tettet med epoxy, men luft ble fremdeles observert i sugerørskonusen. Den innkommende luften resulterte i en overdreven pisk i sugerøret, og derfor er resultatene i dette arbeidet ikke direkte sammenlignbare med tidligere data.

CONTENTS

Acknowledgements	III
Abstract	V
Sammendrag	VII
Contents	VIII
List of Figures	X
List of Tables	XIII
Abbreviations	XIV
Nomenclature	XV
1 Introduction	1
1.1 Background and objectives	1
2 Previous work	3
3 Theory	4
3.1 Pressure fluctuations	4
3.1.1 High frequent pressure pulsations	4
3.1.2 Rotating vortex rope	6
3.1.3 Elastic fluctuations	7
3.2 Model testing	8
3.3 Frequency analysis	9
3.3.1 Discrete sampling and sampling rate	9
3.3.2 Filtering and smoothing data	11
3.3.3 Spectral analysis using Fourier transform	12
3.3.4 Window functions	12

3.3.5	Phase averaging	14
4	Materials and methods	15
4.1	Laboratory facilities	15
4.2	Model runner	16
4.2.1	Calibration	16
4.2.2	Runner sensors	17
4.3	Measurement equipment	17
4.4	Measurement program	19
4.4.1	FPGA.vi	21
4.4.2	Realtime.VI	22
4.5	Operating range for sampling	23
5	Results	25
5.1	Spectral analysis	25
5.1.1	Frequency domain at 100% load	28
5.1.2	Frequency domain at 75% load	32
5.1.3	Frequency domain at 50% load	36
5.1.4	Frequency domain at 45% load	40
5.1.5	Frequency domain at 42% load	44
5.1.6	Generator Torque	46
5.1.7	Draft tube	47
5.1.8	Low frequency regime	48
5.2	Phase averaged	52
5.2.1	Stationary sensors	58
5.2.2	Rotating sensors	61
6	Discussion	62
6.1	Runner frequency	63
6.2	RSI	64
6.3	Rheingans Frequency	66
6.4	Spiral casing	67
6.5	Data aquisition system	68
7	Conclusion	69
8	Further Work	71
	Appendix	74
	Appendix A - Calibration	75
	Appendix B - Defect blade sensors	95
	Appendix C - Rig setup	96
	Appendix D - Air leakage	98
	Appendix E - Compact RIO Installation	99
	Appendix F - Results	100
	Appendix G - Risk assesment	102

LIST OF FIGURES

3.1 Rotor-stator-interaction in a pump turbine. Sensor placement to the right and corresponding amplitudes to the left. [Dorfler et al., 2013].	6
3.2 Rotating vortex rope	7
3.3 Sample frequencies for 350 Hz signal [Thomas Zawistowski, 2013]	10
3.4 Noise is filtered from the original signal (a) by using quadratic S-G (b) and quartic S-G (c).	12
3.5 Spectral resposns of rectangular window [Heinzel et al., 2002]. . .	13
4.1 Setup of Francis rig	15
4.2 Location of sensors on runner blade	16
4.3 Remaining sensors on the runner blade. (Red circles indicated pressure side, blue circles indicates suction side)	17
4.4 Schematic representation of data aquisition system	18
4.5 Schematic representation of sensor locations	19
4.6 Compact RIO software architecture	21
5.1 Frequency domain of pressure sensors in the waterway at 100% load	27
5.2 Frequency domain of pressure sensors in the waterway at 75% load	31
5.3 Frequency domain of pressure sensors in the waterway at 50% load	35
5.4 Frequency domain of pressure sensors in the waterway at 45% load	39
5.5 Frequency domain of pressure sensors in the waterway at 42% load	43
5.6 Frequency domain of the generator torque at various loads . . .	46
5.7 Frequency domain of draft tube sensor at various loads	47
5.8 Low frequency regime of runner sensors, generator torque and draft tube cone at 50% load	48

5.9	Low frequency regime of runner sensors, generator torque and draft tube cone at 45% load	50
5.10	Low frequency regime of runner sensors, generator torque and draft tube cone at 42% load	51
5.11	Angularly resolved data from stationary sensors at 100% load .	53
5.12	Angularly resolved data from stationary sensors at 75% load .	54
5.13	Angularly resolved data from stationary sensors at 50% load .	55
5.14	Angularly resolved data from stationary sensors at 45% load .	56
5.15	Angularly resolved data from stationary sensors at 42% load .	57
5.16	Angularly resolved data of rotating sensors at 100% load . . .	59
5.17	Angularly resolved data of rotating sensors at 75% load	59
5.18	Angularly resolved data of rotating sensors at 50% load	60
5.19	Angularly resolved data of rotating sensors at 45% load	60
5.20	Angularly resolved data of rotating sensors at 42% load	61
6.1	Normalized amplitudes of runner frequency at various loads . .	63
6.2	Normalized amplitudes of the blade passing frequency at various loads	64
6.3	Normalized amplitudes of the guide vane frequency at various loads	64
6.4	Normalized amplitude of the Rheingans frequency at 50%, 45% and 42% load	66
6.5	2 rotations resolved angularly, Sensor P2	67
8.1	Water leaking out of transducers	95
8.2	Setup of Francis rig with sensors in stationary frame	97
8.3	Wire opening filled with epoxy	98
8.4	Compact RIO mounted on shaft	99
8.5	Lower frequency domain at 100% load	100
8.6	Lower frequency domain at 75% load	101
8.7	Phase averaging of runner sensor P2 at 100% load	101

LIST OF TABLES

4.1	Data aquisition system	20
4.2	Measuring equipment	20
4.3	Operating conditions for sampling	23
5.1	Expected frequencies	26
5.2	Rotational frequency of sensors at 100% Load	28
5.3	Blade passing frequency of sensors at 100% Load	28
5.4	Guide vane frequency of sensors at 100% Load	29
5.5	Rotational frequency of sensors at 75% Load	32
5.6	Blade passing frequency of sensors at 75% Load	33
5.7	Guide vane frequency of sensors at 75% Load	33
5.8	Rotational frequency of sensors at 50% Load	36
5.9	Blade passing frequency of sensors at 50% Load	36
5.10	Guide vane frequency of sensors at 50% Load	37
5.11	Rotational frequency of sensors at 45% Load	40
5.12	Blade passing frequency of sensors at 45% Load	40
5.13	Guide vane frequency of sensors at 45% Load	41
5.14	Rotational frequency of sensors at 42% Load	44
5.15	Blade passing frequency of sensors at 42% Load	44
5.16	Guide vane frequency of sensors at 42% Load	45
5.17	Norm. Amplitudes of Generator Torque frequency at various operating conditions.	46
5.18	Norm. Amplitudes of draft tube frequency at various operating conditions.	47
5.19	Norm. Amplitudes of the lower frequency regime in sensors at 50% Load	49
5.20	Norm. Amplitudes of the lower frequency regime in sensors at 45% Load	50
5.21	Norm. Amplitudes of the lower frequency regime in sensors at 42% Load	51

ABBREVIATIONS

BEP	Best efficiency point
CFD	Computational Fluid Dynamics
cRIO	CompactRIO
DFT	Discrete Fourier transform
DMA	Direct Memory Access
FFT	Fast Fourier Transform
FIFO	First in, First out
FPGA	Field Programmable Array
I/O	Input/Output
IRQ	Interrupt Request
NI	National Instruments
NTNU	Norwegian University of science and technology
RSI	Rotor-Stator-Interaction
VI	Virtual Instrument

NOMENCLATURE

a	Speed of sound	[m/s]
σ	Sigma, Plant submergence	[-]
f_n	Runner rotational frequency	Hz
f_s	Logging frequency	Hz
f_N	Nyquist of folding frequency	Hz
f_{bp}	Blade passing frequency	Hz
f_{gv}	Guide vane frequency	Hz
f_R	Rheingans frequency	Hz
H	Head	[mwc]
K	Coefficient of stiffness	[-]
n	Runner rotational speed	[rpm]
n_{ED}	Speed factor	[-]
Q	Flow	m^3/s
Q_{ED}	Flow factor	[-]
Z_{bp}	Number of Runner blades	[-]
Z_{gv}	Number of Guide vanes	[-]

Intermittent energy resources like solar and wind are gradually increasing their share in the global energy market. As a result, grid stability issues arise and grid transients necessitate fast, reliable and high-quality power generation [Trivedi et al., 2013]. Hydropower, with its excellent storage capability and potential for flexible generation, is ideal for maintaining grid stability. Thus, turbines are operated over an extended range, often far from the original design conditions.

During part load operating conditions, fixed-blade runners display a strong swirl at the runner outlet. This phenomenon can generate strong vibrations and noise that can cause fatigue damage over time. This is a well known issue for operation of Francis turbines [Frunzâverde et al., 2010]. Other pressure fluctuations such as Rotor-Stator-Interaction (RSI) and draft tube surges or Rheingans oscillations are also of interest as their influence on plant operation and runner life is still not fully understood.

1.1 Background and objectives

Pressure and strain measurements have been performed on a high head Francis model. This includes on-board measurements implemented in two of the runner blades. Since the field test conditions are known, it is possible to produce similar operational conditions on the model.

The main objectives for this thesis will therefore be the following:

- Set up a data acquisition system that allows for simultaneous sampling of signals from rotating sensors

- Map pressure pulsations and blade stresses at different operating conditions
- Analyze pressure pulsations and stresses caused by Rotor-stator-interaction, draft tube vortex and detachments
- Check for correlation between pressure pulsations in the draft tube and runner channels

The strain gages installed on the runner blade were all defect when the tests started. Therefore, the objective related to the strain gages could not be accomplished.

CHAPTER 2

PREVIOUS WORK

The field of pressure fluctuations in reaction turbines has experienced ongoing research over time. One of the first articles on the subject was submitted by Rheingans on the issue of power swings due to draft tube surges [Rheingans, 1940]. In recent times, The FLINDT project built a large experimental database on partial flow operating regimes by utilising 2D laser doppler velocimetry and 3D particle image velocimetry [Ciocan et al., 2007]. By identifying velocity and pressure in the discharge ring, as well as unsteady wall pressure and friction they were able to compare numerical and experimental results.

During his work as a PhD candidate at NTNU, Kobro tested both prototype and model in an attempt to establish a general connection between pulsations in model and prototype runner [Kobro, 2012]. Master students Haugan [Haugan, 2012] and Tørklep [Tørklep, 2012] have both studied pressure pulsations in high head Francis turbines in connection with their Master thesis at NTNU.

PhD candidate C. Trivedi from the university of Luleå worked with Francis turbine transients and measurements, the goal was to gain better understanding of dynamic pressure phenomena from analysis of measured data.

A project with strong similarities to the scope of this thesis is the work done by Prof. Cervantes on the U9 Kaplan turbine prototype in Sweden. A total of 5 National Instruments slaves cRIO 9014 (3 stationary, 2 mounted on a rotating shaft) and a master computer were utilized to perform simultaneous measurements of over 200 channels at a sampling rate of 2.5kHz [Cervantes et al., 2008].

3.1 Pressure fluctuations

A Francis turbine running at best efficiency point will normally be influenced by oscillations caused by Rotor-stator-interaction. However, when the turbine is operated outside BEP, additional phenomena such as vortex breakdown and separation around curved lines are apparent. The off-design induced pressure phenomena can have large amplitudes that can impose serious threats on structural parts of the runner. The magnitude of these oscillations depend on design, operational patterns and dynamic response of the system. The oscillations can occur periodically or stochastically. It is evident from experimental results that low load oscillations often have a stochastic nature while high load oscillations occur periodically [Seidel et al., 2012].

3.1.1 High frequent pressure pulsations

Pressure distribution on the runner blades will vary from pressure to suction side of the blade to produce the working torque of the runner. This pressure field rotates with the runner and a stationary observer would see periodic variations of pressure and velocity as a result of runner blades passing [Dorfler et al., 2013]. The blade passing frequency is the product of number of runner blades, Z_{bp} and runner rotation frequency f_n .

$$f = \frac{n}{60} [Hz] \quad (3.1)$$

$$f_{bp} = f \cdot Z_{bp} \cdot (m = 1, 2, 3...) \quad [Hz] \quad (3.2)$$

A pressure pulse is generated every time a blade passes a guide vane. The amplitude of this pulse is predominant during steady operation. The amplitude of this frequency will change as the condition of the guide vanes changes. The guide vane passing frequency and its harmonics is determined by the numbers of guide vanes, Z_{gv} and runner rotation frequency f_n .

$$f_{gv} = f \cdot Z_{gv} \cdot (n = 1, 2, 3...) \quad [Hz] \quad (3.3)$$

The amplitude of these pulsations can increase to unfavourable levels if the system experiences hydraulic unbalance. This unbalance is caused by uneven partition of water in the blade flow channels and can have several causes:

- Badly positioned guide vanes during assembly
- Foreign parts caught in the runner channel

The blade passing frequency and guide vane frequency makes up the dynamic pressure phenomena known as the Rotor-Stator-Interaction. The natural frequency of the pulsations caused by RSI can be in the same order of magnitude as the natural frequencies of the structural parts. Therefore, consideration of RSI is essential for mechanical design [Dorfler et al., 2013]. The interaction between impeller vanes and guide vanes is one of the main contributors to vibration and cracking in Francis turbines. Pressure fluctuations protrude upwards towards the spiral casing. Therefore, the most significant fluctuations will occur when the guide vanes are opened in full position as the impeller blades are closest to the trailing edge.

Larger distances between stator and rotor blades increase turbulence mixing and dissipate wakes, thus decreasing RSI effects [Seidel et al., 2012]. This can be observed in Figure 3.1 where point 69 has significantly higher amplitude than point 40 in the far right figure. Medium and low head Francis runners have a considerable distance between rotor and stator. Fluctuations due to blade passing are therefore normally not an issue in these machines.

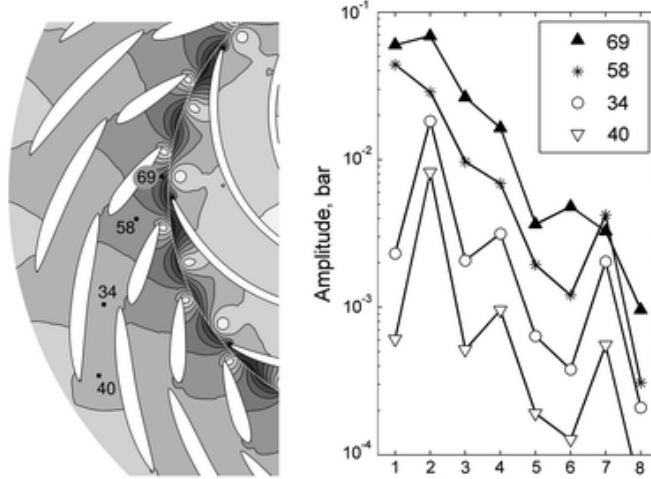


Figure 3.1: Rotor-stator-interaction in a pump turbine. Sensor placement to the right and corresponding amplitudes to the left. [Dorfler et al., 2013].

3.1.2 Rotating vortex rope

The draft tube vortex frequency or Rheingans frequency is only apparent in turbine mode. This frequency is apparent on both sides of the runner which indicates that this is due to mass fluctuation and not elastic impacts as the former frequencies. The draft tube vortex is always present and rotates at 30-50% of the runner speed. However, the amplitude of the generated frequency does not become predominant until the pressure in the vortex drops, creating a visible swirl of vapor inside the draft tube [Rheingans, 1940]. See Figure 3.2.

$$f_R \cong \frac{f}{3,6} [Hz] \quad (3.4)$$

Francis runners are exposed to swirling flow at part load conditions due to their fixed blade design. Swirling can increase performance of draft tube as it prevents separation at cone wall [SENOO et al., 1978]. However, if the flow entering the draft tube experiences high intensity swirl, negative axial velocity can be present in the center of the draft tube and vortex breakdown might occur. These rotating fluctuations combined with synchronous pressure oscillations in the elbow draft tube, causes fluctuations of the pressure level of the draft tube inlet. This works as an excitation to the entire power plant and may set restrictions on the plants operating range [Ruprecht et al., 2002].



Figure 3.2: Rotating vortex rope

3.1.3 Elastic fluctuations

The waterway of a hydropower plant can experience large pressure fluctuations due to system inequalities. Water is elastic and will compress and generate pressure waves when inequalities occur. Thus, fluctuations arise when steady flow of water is interrupted by for example change in guide vane position, or more severe, a sudden closure of the main valve or guide vanes. These dynamic phenomena are not dependent on rotational speed of the runner but rather the geometry of the waterway and the propagation speed of the pressure wave.

$$a = \sqrt{\frac{K}{\rho}} \quad (3.5)$$

If a sudden change in load occurs, a pressure wave will propagate through the water with the speed of sound. The masses of water in the piping system will be decelerated and cause a sudden increase of pressure in front of the main valve. The pressure front will propagate until it reaches a higher free surface reservoir. This phenomena is known as the water hammer oscillation and can occur both upstream and downstream the turbine. The period of the pressure wave (T_w) is four times the length to the nearest free surface reservoir (L), divided by the speed of sound.

$$T_w = \frac{4L}{a} \quad (3.6)$$

$$f_w = \frac{a}{4L} \quad (3.7)$$

When waterhammer occurs, water will be forced through the surgeshafts and on to the upper and lower reservoirs due to differences in free surface water level. This oscillation will continue until friction in the piping system has dampened the effect. This is also referred to as U-tube fluctuations [Nielsen, 1990]. Equations 3.8 and 3.9 denotes the period and frequency of ideal U-tube oscillations with no dampening.

$$T_u = 2\pi\sqrt{\frac{l}{2g}} \quad (3.8)$$

$$f_u = \frac{1}{T_u} = \frac{1}{2\pi\sqrt{\frac{l}{2g}}} \quad (3.9)$$

The speed of sound can vary for the same medium and will have to be defined prior to a frequency analysis of elastic fluctuations. For still water, the speed of sound is approximately 1450 m/s. When taking into account elasticity in pipes, the speed of sound in tunnels and waterways is approximately 1200 m/s. Unfortunately this parameter is not known for the laboratory at NTNU. Thus, there will be some uncertainties when defining the frequencies of elastic fluctuations during tests.

3.2 Model testing

Model testing is an important element in design and development of new turbines. Larger projects usually integrate proof-of-performance testing in contracts. Furthermore, experience has shown that competitive model testing at independent laboratories can lead to substantial savings due to improved efficiency. Today's sophisticated numerical analysis of flow characteristic require fine tuning with model tests. This kind of testing is necessary for determining performance over a range of operating conditions and quasistationary characteristics [Arndt, 1990].

Extrapolation of results from model to prototype has been and still is of considerable debate. Dimensionless numbers like specific speed (Eq. 3.10) and specific flow (Eq. 3.11) are used to predict prototype values of flow, speed, power etc [Arndt, 1990].

$$N_{ED} = \frac{nD}{\sqrt{gH}} \quad (3.10)$$

$$Q_{ED} = \frac{Q}{D^2\sqrt{gH}} \quad (3.11)$$

The dimensionless numbers are based on inviscid flow and describes specific combinations of operating conditions. Hence, they ensure similar flow patterns and same efficiency in geometrically similar machines regardless size and rotational speed. It is customary to define these numbers in terms of the value of the design head and flow at best efficiency point.

The IEC 60193 and various ASME publications gives a detailed outline of the difference in efficiency between model and prototype. It is worth noting that losses such as draft tube and shock at the runner inlet might not be independent of Reynolds number [Arndt, 1990].

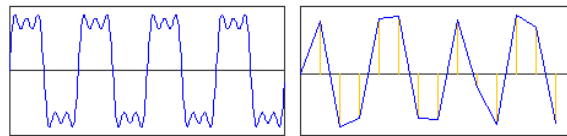
3.3 Frequency analysis

The frequency of a pure sine wave signal is easy to determine. However, most time-varying signals have complex waveforms consisting of a set of sine or cosine waves of different frequencies. The process of determining these frequencies is called spectral analysis. It may be necessary to perform spectral analysis several times when working with time-varying signals. First, in order to determine the sampling rate required. This is done by establishing the frequency characteristics of the measurand. It is possible to utilize data from similar experiments in order to determine the frequency specifications. Secondly, spectral analysis is performed on the acquired data in order to obtain the frequency spectrum. In many time-varying experiments, this is one of the primary results [Wheeler, 2004].

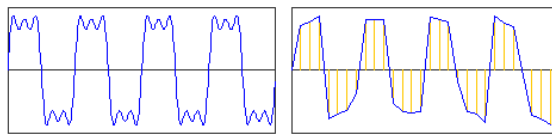
3.3.1 Discrete sampling and sampling rate

While systems record signals continuously through time, digital data-acquisition systems record signals at discrete times. This results in a deduction of actual measured behaviour between samples. The rate at which the measurements are made is referred to as the sampling rate. Choosing an unfit sampling rate can lead to misleading results when analyzing time-varying data. Incorrect or "false" frequencies that appear in data are called aliases. Figure 3.3 displays different sample frequencies for a 350 Hz signal. At 100 Hz and 200 Hz the sample rate is too low and information on the original signal is lost. The reconstruction of this signal will therefore contain unwanted components that

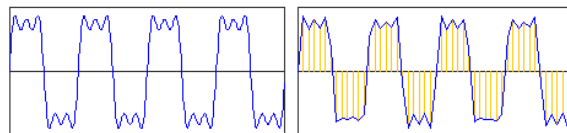
does not originate from the original signal. At 350 Hz the sampling frequency is sufficient and the reconstruction of the original signal will be correct.



(a) 100 Hz sampling frequency



(b) 200 Hz sampling frequency



(c) 350 Hz sampling frequency

Figure 3.3: Sample frequencies for 350 Hz signal [Thomas Zawistowski, 2013]

In order to avoid these aliasing effects the sampling rate f_s has to be at least twice the size of the highest known frequency f_m in the signal. This is referred to as the Nyquist theorem (also known as sampling rate theorem) [Wheeler, 2004].

$$f_s > 2f_m \quad (3.12)$$

The highest frequency components in a signal can often originate from noise. In order to avoid aliasing of these components it is common to filter them out. The activity of blocking out the noise and only letting the lower frequencies through is known as low pass filtering [Thomas Zawistowski, 2013]. Low pass filtering can be done by eliminating noise during sampling. The lowest frequency of a pure signal is known as the fundamental frequency. This is also the first harmonic of the signal. Harmonics are multiples of the fundamental frequency.

3.3.2 Filtering and smoothing data

A moving average data filter smooths points by replacing each point with the average of the neighboring data points defined within a certain span. This process is equivalent to lowpass filtering and the response of the smoothing is given by the difference equation:

$$y_s(i) = \frac{1}{2N + 1} (y(i - N) \dots + y(i) + \dots y(i + N)) \quad (3.13)$$

where $y_s(i)$ is the smoothed value for the i th data point, N is the number of neighboring data points on either side of $y_s(i)$, and $2N + 1$ is the span. The Savitzky-Golay filter is a generalization of the moving average method where the coefficients are derived by conducting an unweighed linear least-square fit using a polynomial of a certain degree [Mathworks, 2013]. The *sgolayfilter* function is available in the Curve Fitting Toolbox in MATLAB R2013a and is based on the following algorithm:

$$y_s(i) = \frac{\sum_{i=-n}^n A_i y_{k+i}}{\sum_{i=-n}^n A_i} \quad (3.14)$$

for $A_{-n}, A_{-(n-1)}, \dots, A_n, A_{(n-1)}$

- The span of points must be odd
- The polynomial degree must be less than the span.
- Data points are not required to have uniform distribution

Higher degree polynomials make it possible to achieve a high level of smoothing without damaging vital data. This filter is often used with frequency as the method is effective for preserving the high frequency components of the signal. Though the method is good at preserving the peaks, it can be less successful at rejecting noise. The use of higher degrees of polynomials can more accurately capture height and widths of narrow peaks but will have problems with smoothing wider peaks. Fig 3.4 displays an example of smoothing a high noise signal with Savitzky-Golay method where the span is 5% of the number of data points.

Though the method is effective for removing noise from data, it will always lead to a certain degree of loss of information and distortion of signal.

It is therefore important to evaluate the parameters when filtering a signal [Mathworks, 2013].

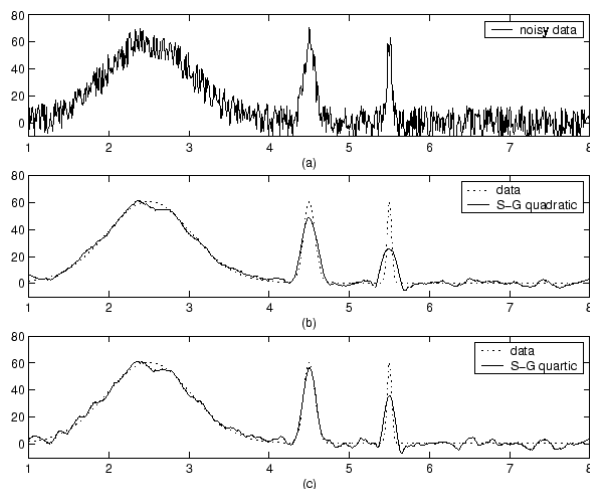


Figure 3.4: Noise is filtered from the original signal (a) by using quadratic S-G (b) and quartic S-G (c).

3.3.3 Spectral analysis using Fourier transform

Fourier analysis is applied to periodic phenomena and represents complicated functions by sine and cosine expressions. These expressions constitutes the infinite series known as the Fourier series. Fourier transform is a generalization of Fourier series and can be applied to any practical function. Discrete data can be evaluated quickly using a modern computer technique called Fast Fourier Transform, often referred to as FFT. The data obtained in this thesis is evaluated by Welch method where a discrete Fourier transform (DFT) is applied to a segment of a time series, modified by a time-domain window and averaged in order to reduce the variance of spectral estimates [Heinzel et al., 2002]. A proper introduction to the theory of Fourier transform and Welch method is displayed excellently in respectively [Wheeler, 2004] and [Heinzel et al., 2002] and will not be included in this thesis.

3.3.4 Window functions

If DFT is performed directly on a sinusoidal signal, the frequency spectrum will appear as something similar to fig 3.5. This is due to the fact that DFT assumes infinite signals. If the frequency of sinusoidal input is not an exact multiple of the frequency resolution, it does not fall in the exact center of the

frequency bin. DFT interprets the discontinuity between the first and last sample and as a consequence, power is spread across the spectrum. This is also referred to as spectral leakage.

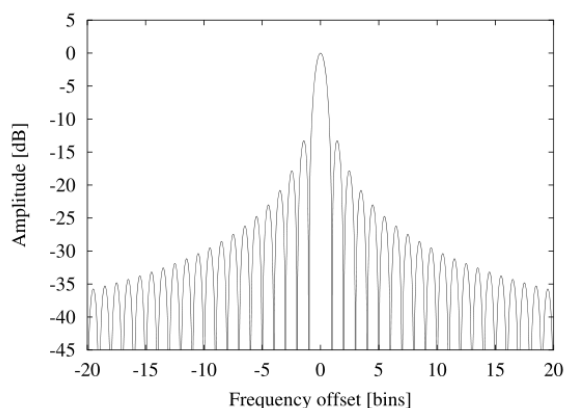
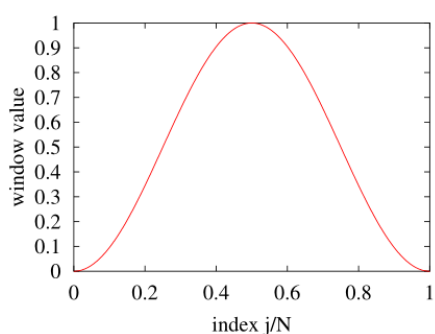
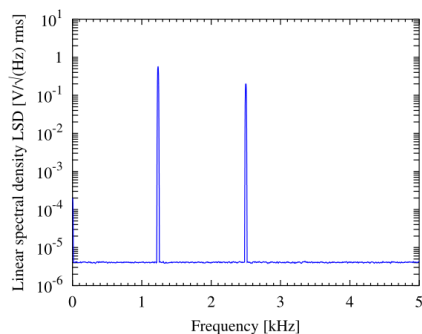


Figure 3.5: Spectral response of rectangular window [Heinzel et al., 2002].

The remedy for this phenomena is to multiply the time series with a window function prior to DFT application. The window function starts around zero, increases to a maximum at center and decreases again. This removes the discontinuity and decreases the rate of spectral leakage into other frequency bins. One can therefore observe clear peaks in the frequency domain. There are several types of window functions. Due to its simple but useful features, the hanning window is often chosen (see Figure 3.6a).



(a) Hanning window in time domain [Heinzel et al., 2002].



(b) Frequency peaks [Heinzel et al., 2002].

3.3.5 Phase averaging

A random process can be described at any instant of time by calculating the average values over the collection of sample functions. If the averaged values depend on time they are referred to as nonstationary, otherwise they are known as stationary. Phase averaging is applied to a specific group of nonstationary random processes with periodic intervals at finite timeseries τ_0 . Averages of these nonstationary random processes are calculated from the sum over discrete instants of times. These discrete times differ by an integer of the multiple τ_0 .

In bin averaging, the period of τ_0 is subdivided into elementary intervals in what are known as bins. The center of each bin is marked by a phase angle in the range of $0-2\pi$. Thus, phase averages are computed from all samples that belong to the separate bins. Bin averaging performs well on measurements with a large number of samples, but exaggerated smoothing of gradients may appear if sample size is too small. Whenever applied, phase averaging should be used with care as the averaging process in general will underestimate high frequency components [Sonnenberger et al., 2000].

4.1 Laboratory facilities

The Francis test rig at the waterpower laboratory holds international standards according to IEC 60193 and can be operated in pump and turbine mode. Testing of the model turbine will be executed in a closed loop. A schematic representation of the setup is displayed in figure 4.1.

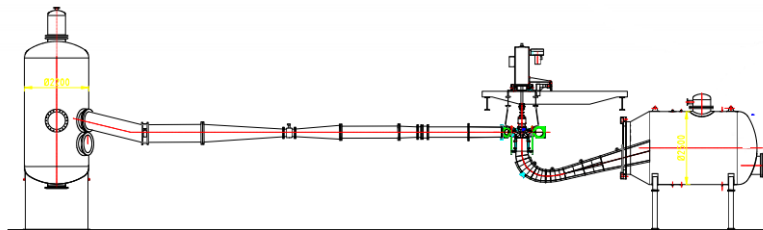


Figure 4.1: Setup of Francis rig

The model turbine is mounted on a vertical shaft with a 352 kW generator. Pressure is generated from a head tank with a diameter of 2.25 meter and a height of 4 meters. The volume of the tank is 18 m^3 for 10 bar pressure at 50°C . The discharge is sent into a tail tank with free water surface that serves as the lower reservoir of the closed loop. The low pressure tank has a capacity of 7 m^3 and a vacuum pump enables evacuation of air during operation. The flow is recirculated by pumps installed in the basement to ensure cavitation-free performance of the pump while performing cavitation testing on the turbine model. The pumps can deliver maximum 100 mwc if run in series. Only one

of the pumps will be needed in this experiment as the maximum model test head is 30.45 mwc. The maximum flow rate of the loop is 1 m^3 . The loop is closed and water will not enter the loop when air is evacuated. The water level of the tail tank will not rise since water at low and moderate pressures is incompressible. Hence, one is able to reach specified operating conditions, using a vacuum pump for sigma variation [Storli, 2006].

4.2 Model runner

The runner consist of seventeen full blades that are screwed individually into the main hub. The model has a diameter of 367.18 mm. A total of 18 pressure transducers of the type Kulite LL-080 Series / LL-125 Series with an operational mode of 17 bars absolute are integrated in one of the runner channels. This is done by milling out parts of the blade and filling the gap with cyanoacrylate to ensure a smooth surface across the blade and preventing water from entering the transducers. 4 full bridge strain gages are fastened to a single blade.

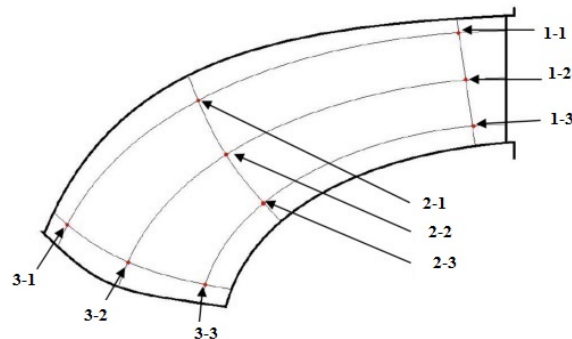


Figure 4.2: Location of sensors on runner blade

4.2.1 Calibration

The runner transducers were calibrated using a pressurized tank. The runner is lowered into the tank and the transducer wires are led out through a specially designed nut filled with a rubber plug. Pressure is increased with a manual pump and recorded by a reference transducer of the type Druck PTX 1400, 0-4 barg. A NIdaq unit, an amplifier set to 5V and a computer with LabVIEW were used for logging signals from the transducers.

A new calibration program was made in order to sample all signals simultaneously. Pressure was sampled for 1.5 seconds with a sampling rate of 1500 samples per second. The output from labview was a 19 column .csv file with 1500 samples. This was again imported to MATLAB in order to obtain the linear equation and the uncertainty band (MATLAB script can be found in the digital Appendix).

4.2.2 Runner sensors

After the measurements were completed it was apparent that only 5 of the runner blade sensors were functional. Figure 4.3 displays an overview of the sensors and their position.

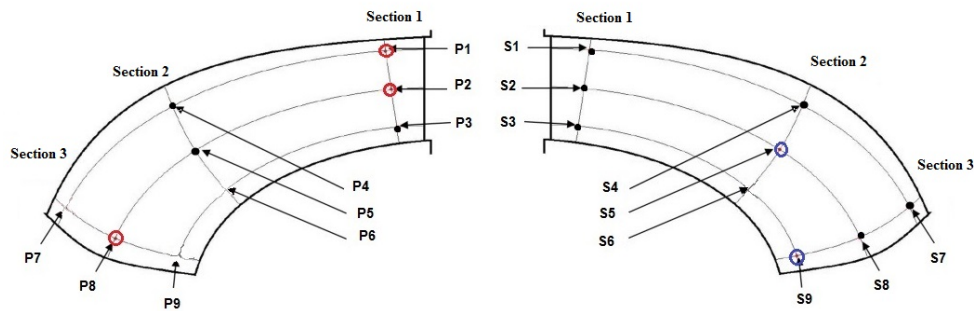


Figure 4.3: Remaining sensors on the runner blade. (Red circles indicated pressure side, blue circles indicates suction side)

4.3 Measurement equipment

In order to perform simultaneous sampling of multiple sensors, National Instruments software (LabVIEW 2012) and Compact RIO controller were chosen. cRIOs compact hardware of 929 grams, excluded modules is suitable for installation on a rotating shaft (see Appendix D for pictures of installation). The cRIO can perform simultaneous sampling on several channels at a rate up to 5000 samples per second.

Two cRio-9074 chassis are utilized together with different modules depending on the incoming signal. The Kulite LL-080 Series / LL-125 Series transducers are logged by 6 NI 9237 modules at a sample rate of 2000 samples per second.

Figure 4.4 describes the data acquisition system.

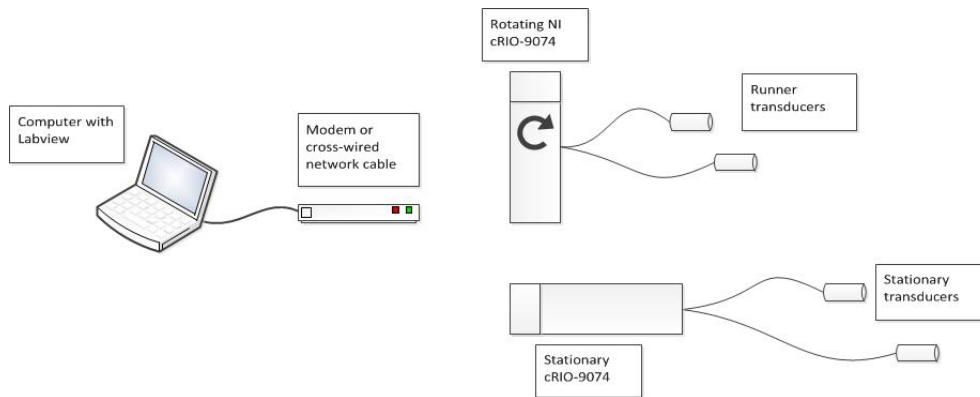


Figure 4.4: Schematic representation of data acquisition system

A stationary system was used to record pressure in inlet, vaneless space and draft tube. Three transducers of the type Druck PTX 610 were placed 3940mm and 870 mm from the inlet of the spiral casing and at the inlet of the tail tank. These were logged with a NI9237 module at a sample rate of 2k samples per second. Three Kulite XTL-190 were flush mounted in the lower part of the spiral casing block for measurements in the vaneless space. Three piezoelectric sensors of the type Kistler 601A were mounted with 90 deg spacing into the draft tube cone. Together with an optical sensor and generator torque these signals were logged using 2 NI9239 modules and logged at 2ks/S. Figure 4.5 describes the angular placement of draft tube sensors, vaneless space sensors and the reference points for the keyphasor and the rotating sensors. These values are important to keep in mind when interpreting the phase averaged data. A schematic representation of the rig setup is available in Appendix C.

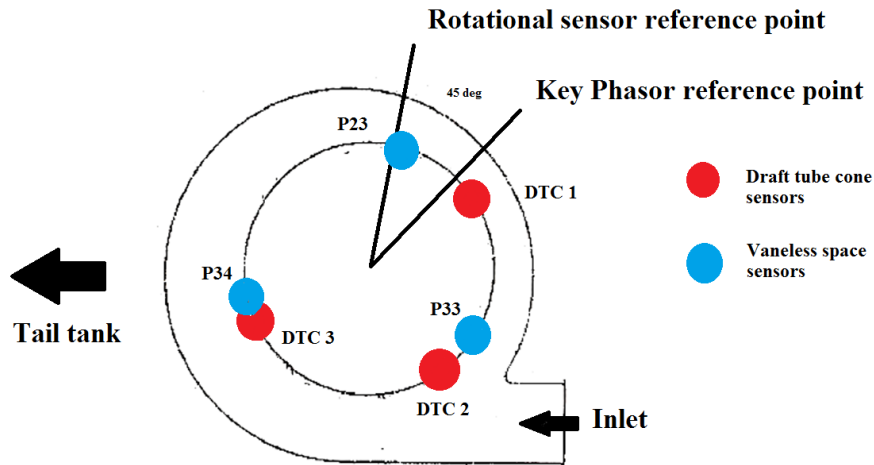


Figure 4.5: Schematic representation of sensor locations

cRIO hardware is suitable for input/output (I/O) communication as it can be programmed to sample and store data to file independently. The cRIOs in this experiment were running a real-time program continuously. The program was writing a certain amount of samples to file when triggered. The trigger signal was transferred to the rotating cRIO through a slip ring assembly together with the power supply of the cRIO. Signal from a keyphasor was transferred to both cRIOs and used as a reference to adjust the signals in the rotating and stationary frames of references allowing a nearly simultaneous sampling.

4.4 Measurement program

Programming on cRIO can be separated into two main categories. Firstly, a main VI (virtual instrument) that executes the sampling must be created by FPGA (Field programmable array). FPGAs are basically programmable silicon chips, and programming on FPGA rewrites the silicon chips to implement functionality rather than running software [Instruments, 2013b]. The rewiring occurs when graphical programming on the .VI is "translated" and the program is compiled on to the unit by the xilinx 13.4 tool. This type of direct programming ensures faster I/O response times for a sampling system. The FPGA can be controlled through a real-time VI that is often referred to as the host VI. This runs in a normal priority loop and can communicate with

Hardware	Type	Range	Bandwidth
PC with Labview	National instruments labview v12.0	Programmable	50 ks/S
I/O controller	National Instruments cRIO-9074	19-30V	
4-Channel, 24-Bit Analog Input Module	NI 9239	-10 V - 10 V	50 kS/s
4-Channel, 24-Bit Simultaneous Bridge Module	NI 9237	-25 mV/V - 25 mV/V	50 kS/s
Removable Storage Module	NI 9802		

Table 4.1: Data acquisition system

Transducer	Range [bar a]	Natural frequency	Quantity	Location
Kulite LL-080 \ LL-125	0-17	550 kHz	18	Runner blade
Kistler 601A	0-250	150 kHz	3	Draft tube cone
Kulite XTL-190	0-7/0-3.5	380/300kHz	3	Vaneless space
Druck PTX 610	0-2.5		3	Upstream \ Downstream inlet

Table 4.2: Measuring equipment

the FPGA part of the unit. Figure 4.6 gives a schematic representation of the software architecture.

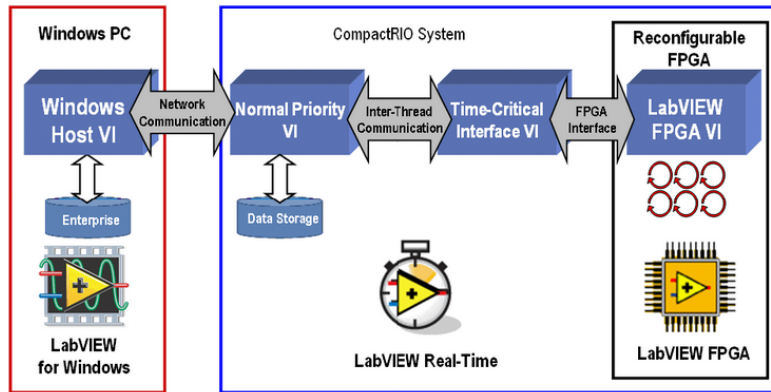


Figure 4.6: Compact RIO software architecture
[Instruments, 2013a]

4.4.1 FPGA.vi

The FPGA programs were controlled by a flat sequence structure that ensures sequentially execution of subdiagrams. Labview files `FPGA_rotating_triggered_1.VI` and `FPGA_stationary_triggered_1.VI` can be found in the digital Appendix.

The sequential structure of the program is listed below:

1. Recieves an interrupt request, also known as an IRQ from the host.VI. Once the host.VI acknowledges the IRQ the sequence continues
2. Data rate and excitation voltage is read from host.VI and settings are executed
3. Starts up modules and is now ready for sampling
4. Standby for trigger signal
5. Sampling starts and data is written to an FPGA FIFO. FIFO stands for first in, first out and sorts elements in the order they are recieved.
6. Stops modules and sequence starts from top.

4.4.2 Realtime.VI

The real-time.VI controls the FPGA program and make sure that everything is executed at the right time and that data is written to files. Labview files Realtime_rotating_triggered_1.VI and Realtime_stationary_triggered_1.VI can be found in the digital Appendix. The host.VI is built and deployed on the cRIO and will run independently on the unit until it is timed out or stopped from a host computer. This is how the rotating cRIO can record data from the rotating shaft without being connected to an external device. The Real-time program is executed in a loop that run every time the cRIO recieve a trigger signal. The loop is not sequenced like the FPGA.VI and several operations will occur simultaneously. The tasks performed by the program are described below:

- Open FPGA reference and execute read/write control on the modules
- Send an IRQ signal in order to synchronize FPGA.VI and host.VI
- Generate interrupts from FPGA.VI to inform host.VI that the system is ready for sampling
- Standby for trigger signal
- Perform read/write control and specify sampling time for FPGA.VI
- Create 1D array and reads DMA (direct memory access) from FPGA FIFO. (The DMA allows FPGA to use the host RAM as its own, resulting in a significant performance enhancement for the system.)
- Transfers data from 1D to 2D array to enable transport of data to file
- Data is streamed to a .tdms file with named specified by day.month.year_hour.minute.second.
- When all the data is transferred, the file closes and restarts the FPGA reference. Is now ready for triggering.

4.5 Operating range for sampling

The tests will be performed with a constant model speed n . 240 000 data points (120 seconds, 2000 samples/second) will be sampled at the operating conditions specified in Table 4.3. The frequency resolution is approximately 0.0083 Hz.

Operational point	Load (%of <i>BEP</i>)
1	100
2	75
3	50
4	45
5	42

Table 4.3: Operating conditions for sampling

5.1 Spectral analysis

This section presents the various frequency domains throughout the waterway. The `pwelch` function in MATLAB was used for spectral analysis, with a Hanning window and an overlap of 50 %. The MATLAB scripts utilized for spectral analysis, phase averaging and plotting are available in the digital Appendix.

The individual dataseries were divided into three timeseries and spectral analysis was performed on each serie and compared to the frequency domain of the entire datarange. This was to ensure consistency throughout the dataseries and avoid irregularities in the frequency domain. It should be stressed that the absolute values of the amplitudes obtained in this method can have large uncertainties. The uncertainties arise when the signal that is processed is both periodic and stochastic, rather than pure sine signals. However the method is considered suitable for the relative comparison that will be performed on the presented results.

Figure 5.1 displays the predominant frequencies for the stationary and rotating sensors in the order they appear in the waterway. A more detailed description of the frequency domain will be presented in a later section. All frequencies will henceforth be normalized with respect to the runner frequency. Amplitudes are also normalized, but the normalization factor will not be disclosed due to confidentiality of the model properties.

The most predominant frequencies expected to be found from testing of the model runner are displayed in table 5.1.

Frequency	[Hz]	$\frac{f}{f_n}$ [-]
Runner frequency	9	1
Blade passing frequency	153	17
Guide vane frequency	252	28
Rheingans frequency	2.5	≈ 0.3

Table 5.1: Expected frequencies

There is also an expected frequency of approximately 96Hz (10.67), with its half (48Hz) (5.33), second (192Hz) (21.33) and third harmonic (288Hz) (32) that has been apparent during former model tests at the waterpower laboratory. This frequency is assumed to arise from elastic fluctuations and is independent of runner rotational speed. Further discussion of its origin can be found in [Tørklep, 2012] chapter 5.3.3.

The following section contains waterfall plots of the frequency domain of sensors in the waterway at 100%, 75%, 50%, 45% and 42% load. The Z-axis is in logarithmic scale. Due to the amount of data in this plot, the angle is adjusted in order to cover all peaks. Therefore, the x-axis appears to be shifted and frequencies appear lower than their actual values. Numerical values (not logarithmic) of the frequencies and amplitudes of interest will therefore be presented in tables. The corresponding MATLAB figure files are available in the electronic Appendix and it is recommended to study the figure more closely here. Due to the nature of their data, the frequency domain of the draft tube sensor and generator torque will be presented in separate figures.

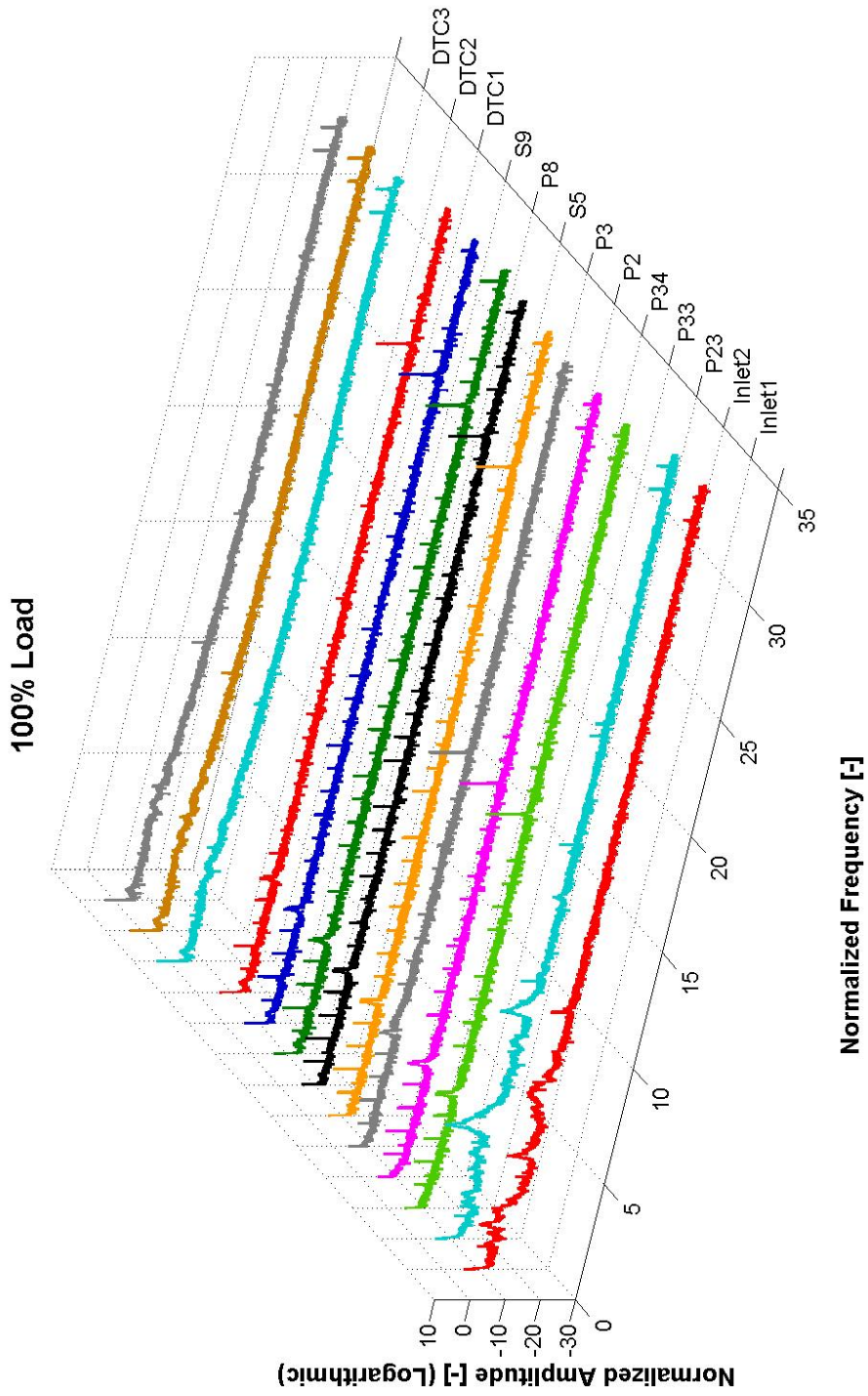


Figure 5.1: Frequency domain of pressure sensors in the waterway at 100% load

5.1.1 Frequency domain at 100% load

The runner frequency is apparent in Figure 5.1 as the first peak on the x-axis. The numerical values of the runner frequency and the normalized amplitudes of the sensors are presented in Table 5.2. The draft tube cone sensors does not display a clear peak at 1 and are therefore not included.

Sensor	Norm. Amplitude [-]
Inlet 1	3.85e-09
Inlet 2	2.11e-10
P23	1.33e-06
P33	9.22e-06
P34	4.8e-06
P2	7.76e-08
P3	2.34e-06
S5	1.11e-10
P8	9.46e-10
S9	2.19e-11

Table 5.2: Rotational frequency of sensors at 100% Load

The blade passing frequency is visible as dominant peaks in sensors P23, P33 and P34. It is also present as smaller peaks in other sensors. The numerical values of the blade passing frequency and the normalized amplitudes of the sensors are presented in Table 5.3.

Sensor	Norm. Amplitude [-]
Inlet 2	8.12e-14
P23	1.7
P33	0.61
P34	7.03
P2	8.39e-10
P3	1.08e-10
S5	8.7e-12
P8	5.75e-12
S9	1.95e-12

Table 5.3: Blade passing frequency of sensors at 100% Load

The guide vane frequency is visible as dominating peaks in the runner sensors. The numerical values of the guide vane frequency and the normalized amplitudes are presented in Table 5.4.

Sensor	Norm. Amplitude [-]
P2	2.41e-03
P3	6.98e-03
S5	4e-04
P8	1.85e-04
S9	1.54e-05

Table 5.4: Guide vane frequency of sensors at 100% Load

The harmonics of the runner frequency is apparent in the frequency domain. 4.9, 32.33 and 33.32 are present throughout the system and will be discussed in detail later. 11.11 is apparent at the inlet and in the draft tube cone.

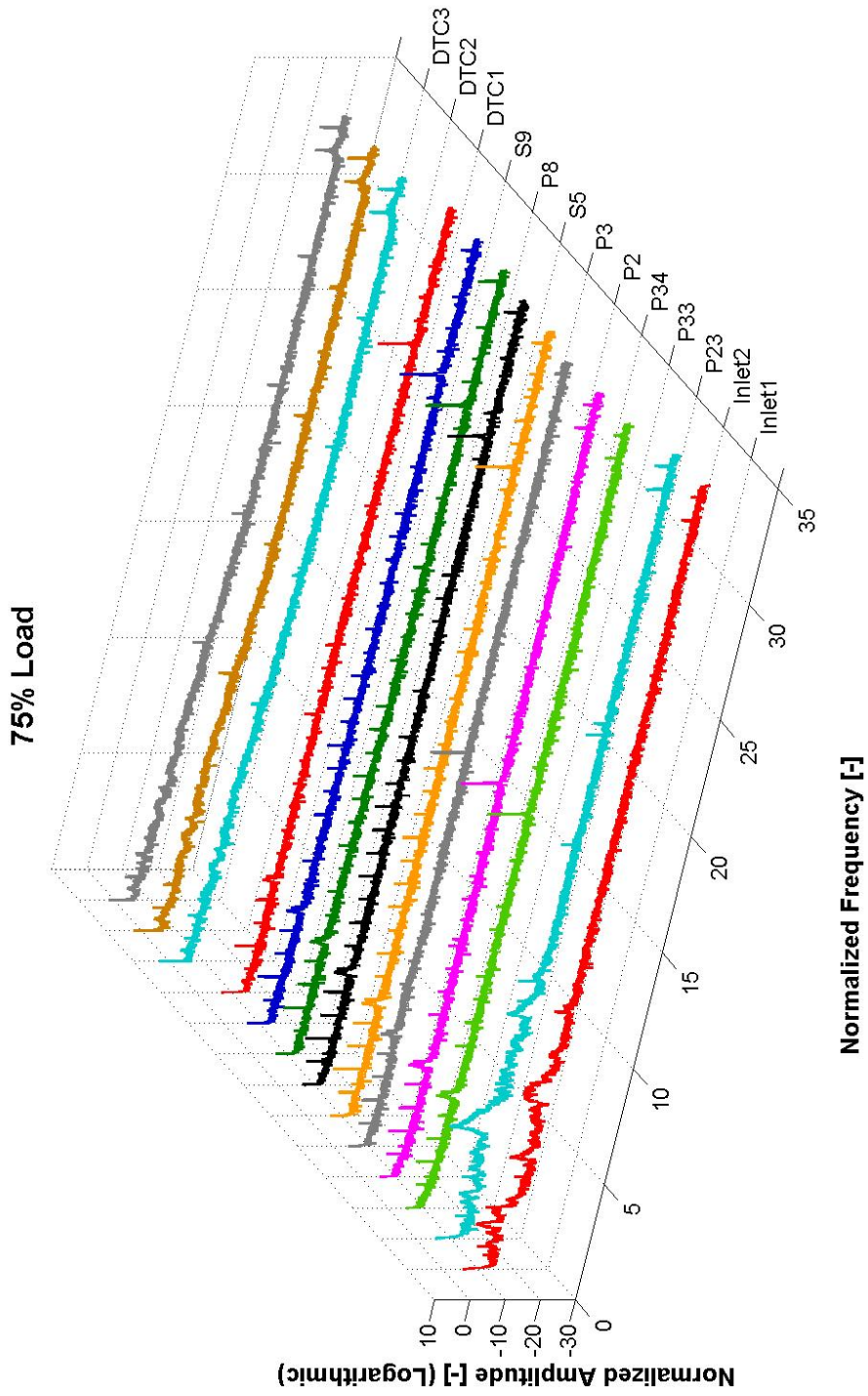


Figure 5.2: Frequency domain of pressure sensors in the waterway at 75% load

5.1.2 Frequency domain at 75% load

The runner frequency is apparent in Figure 5.2 as the first peak on the x-axis. The numerical values of the runner frequency and the normalized amplitudes of the sensors are presented in Table 5.5.

Sensor	Norm. Amplitude [-]
Inlet 1	4.49e-09
Inlet 2	1.46e-10
P23	2.81e-07
P33	1.95e-06
P34	1.97e-06
P2	2.05e-08
P3	4.72e-07
S5	2.63e-11
P8	1.79e-10
S9	1.45e-12
DTC1	2.32e-03
DTC2	0.032
DTC3	0.037

Table 5.5: Rotational frequency of sensors at 75% Load

The blade passing frequency is visible as predominant peaks in sensors P23, P33 and P34. It is also present as smaller peaks in other sensors. The numerical values of the blade passing frequency and the normalized amplitudes of the sensors are presented in Table 5.6.

Sensor	Norm. Amplitude [-]
Inlet 2	2.29e-14
P23	0.373
P33	0.833
P34	2.588
P2	4.26e-12
P3	3.47e-11
S5	3.09e-12
P8	4.9e-13
S9	7.08e-14

Table 5.6: Blade passing frequency of sensors at 75% Load

The guide vane frequency is visible as dominating peaks in the runner sensors. The numerical values of the guide vane frequency and the normalized amplitudes are presented in Table 5.7.

Sensor	Norm. Amplitude [-]
P2	7.69e-03
P3	0.013
S5	3.72e-04
P8	1.12e-04
S9	3.11e-06

Table 5.7: Guide vane frequency of sensors at 75% Load

Draft tube sensors DT1, DT2 and DT3 display the guide vane frequency at 27.78 with 2.8e-08, 3.99e-08 and 5.51e-07 respectively.

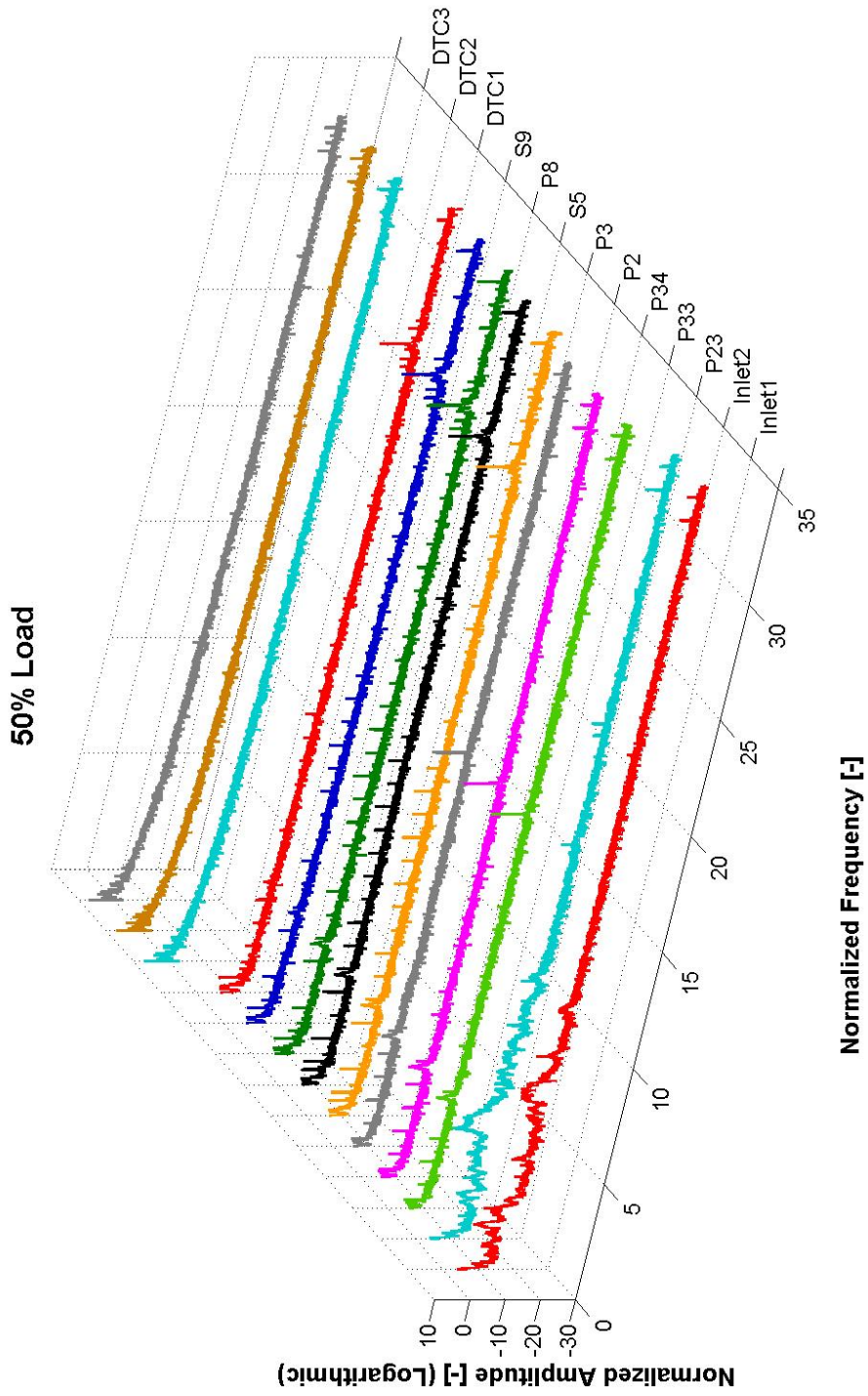


Figure 5.3: Frequency domain of pressure sensors in the waterway at 50% load

5.1.3 Frequency domain at 50% load

The runner frequency is apparent in Figure 5.3 as the first peak on the x-axis. The numerical values of the runner frequency and the normalized amplitudes of the sensors are presented in Table 5.8.

Sensor	Norm. Amplitude [-]
Inlet 1	4.68e-10
Inlet 2	3.02e-11
P23	1.01e-07
P33	4.88e-07
P34	7.21e-08
P2	3.05e-06
P3	4.72e-07
S5	3.33e-06
P8	9.04e-10
S9	5.97e-10

Table 5.8: Rotational frequency of sensors at 50% Load

The blade passing frequency is visible as dominant peaks in sensors P23, P33 and P34. It is also present as smaller peaks in other sensors. The numerical values of the blade passing frequency and the normalized amplitudes of the sensors are presented in Table 5.9.

Sensor	Norm. Amplitude [-]
Inlet 2	2.19e-14
P23	0.04
P33	0.029
P34	0.667
P2	5.13e-12
S5	1.02e-13
P8	1.38e-14
S9	1.78e-14

Table 5.9: Blade passing frequency of sensors at 50% Load

The guide vane frequency is visible as dominating peaks in the runner sensors. The numerical values of the guide vane frequency and the normalized

amplitudes are presented in Table 5.10.

Sensor	Norm. Amplitude [-]
P2	3.89e-03
P3	7.03e-03
S5	1.84e-04
P8	4.52e-05
S9	3.22e-06

Table 5.10: Guide vane frequency of sensors at 50% Load

Draft tube sensor DT3 display the guide vane frequency at 27.78 with 9.98e-07.

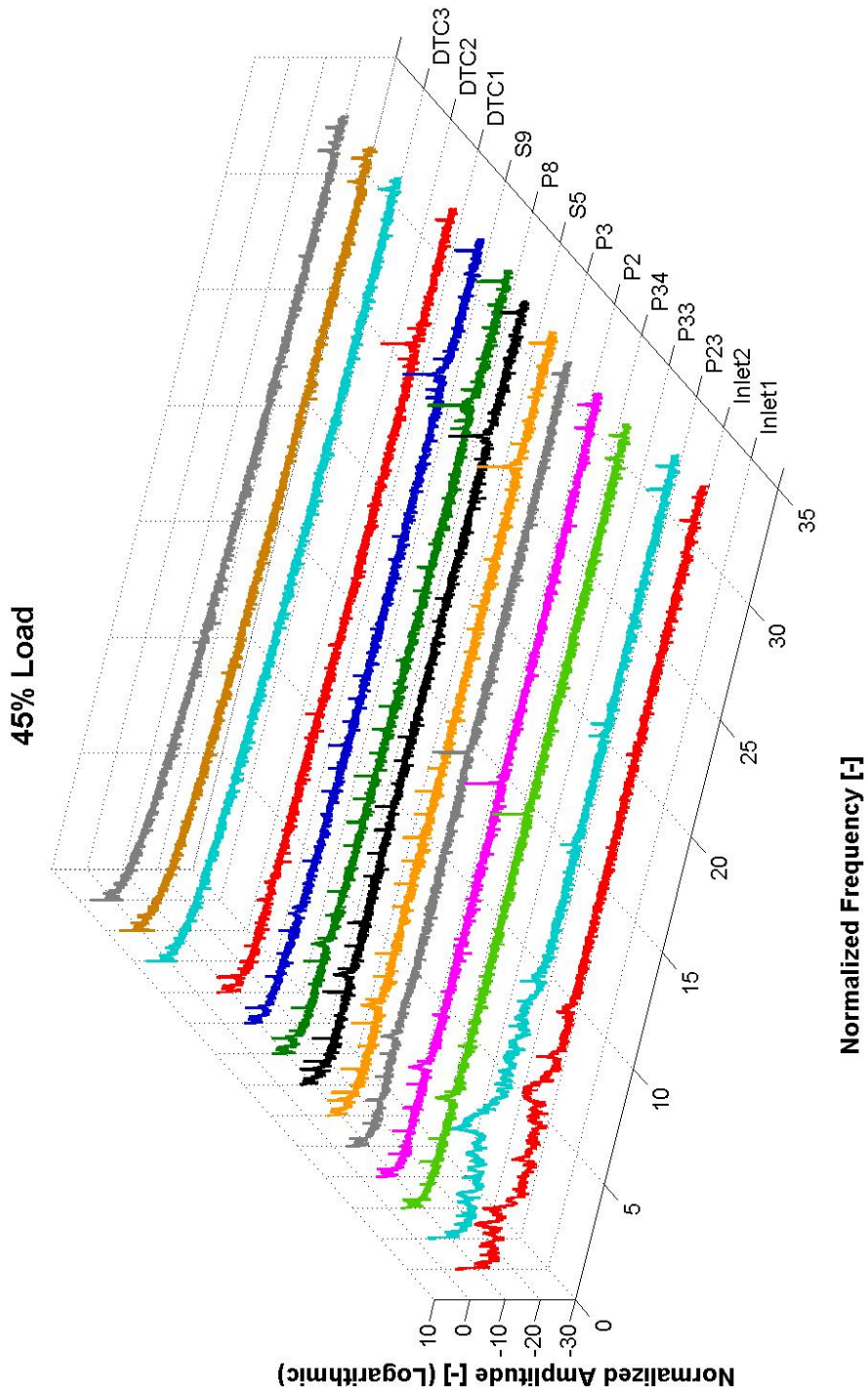


Figure 5.4: Frequency domain of pressure sensors in the waterway at 45% load

5.1.4 Frequency domain at 45% load

The runner frequency is apparent in Figure 5.3 as the first peak on the x-axis. The numerical values of the runner frequency and the normalized amplitudes of the sensors are presented in Table 5.8.

Sensor	Norm. Amplitude [-]
Inlet 1	1.21e-09
Inlet 2	8.32e-11
P23	2.62e-08
P33	3.43e-07
P34	1.61e-07
P2	3.07e-06
P3	2.56e-06
S5	3.33e-06
P8	4.82e-10
S9	7.41e-11

Table 5.11: Rotational frequency of sensors at 45% Load

The blade passing frequency is visible as dominant peaks in sensors P23, P33 and P34. It is also present as smaller peaks in other sensors. The numerical values of the blade passing frequency and the normalized amplitudes of the sensors are presented in Table 5.12.

Sensor	Norm. Amplitude [-]
Inlet 2	7.24e-14
P23	5.09e-03
P33	0.02
P34	0.52
P2	1.62e-12
S5	7.41e-14
P8	3.31e-14

Table 5.12: Blade passing frequency of sensors at 45% Load

The guide vane frequency is visible as dominating peaks in the runner sensors. The numerical values of the guide vane frequency and the normalized amplitudes are presented in Table 5.13.

Sensor	Norm. Amplitude [-]
P2	3.23e-03
P3	6.74e-03
S5	9.57e-05
P8	2.13e-05
S9	5.98e-07

Table 5.13: Guide vane frequency of sensors at 45% Load

Draft tube sensor DT3 display the guide vane frequency at 27.78 with 3.81e-07.

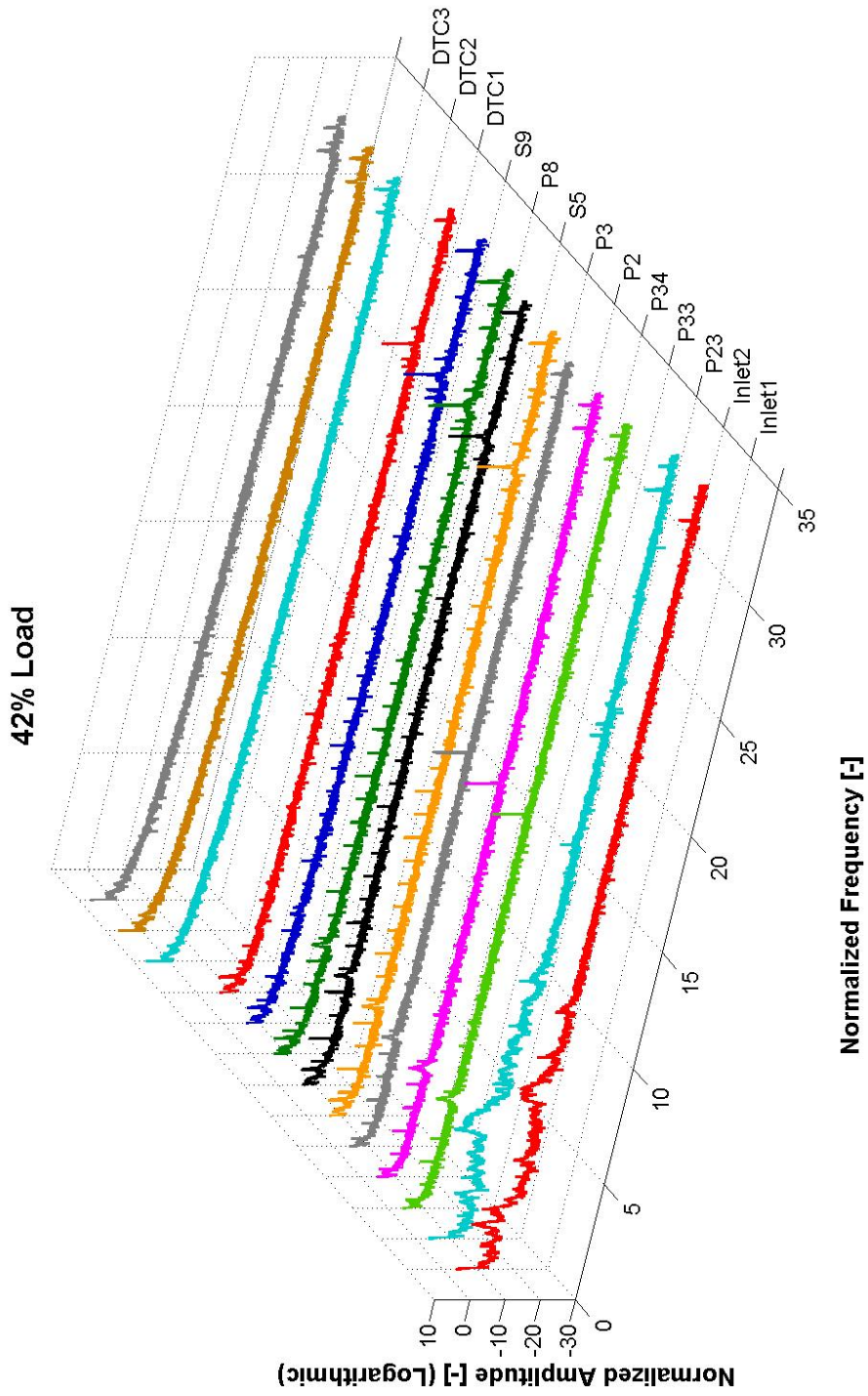


Figure 5.5: Frequency domain of pressure sensors in the waterway at 42% load

5.1.5 Frequency domain at 42% load

The runner frequency is apparent in Figure 5.3 as the first peak on the x-axis. The numerical values of the runner frequency and the normalized amplitudes of the sensors are presented in Table 5.8.

Sensor	Norm. Amplitude [-]
Inlet 1	7.5e-10
Inlet 2	5.49e-11
P23	2.95e-08
P33	9.42e-08
P34	2.53e-07
P2	3.52e-08
P3	1.4e-08
S5	4.98e-08
P8	1.56e-08
S9	1.31e-10

Table 5.14: Rotational frequency of sensors at 42% Load

The blade passing frequency is visible as dominant peaks in sensors P23, P33 and P34. It is also present as smaller peaks in other sensors. The numerical values of the blade passing frequency and the normalized amplitudes of the sensors are presented in Table 5.15.

Sensor	Norm. Amplitude [-]
Inlet 2	5.75e-14
P23	2.45e-03
P33	0.014
P34	0.42
P2	1.02e-12
S5	5.75e-13
P8	1.05e-14
S9	6.17e-15

Table 5.15: Blade passing frequency of sensors at 42% Load

The guide vane frequency is visible as dominating peaks in the runner sensors. The numerical values of the guide vane frequency and the normalized

Sensor	Norm. Amplitude [-]
P2	3.56e-03
P3	6.15e-03
S5	6.35e-05
P8	1.16e-05
S9	7.21e-07

Table 5.16: Guide vane frequency of sensors at 42% Load

amplitudes are presented in Table 5.16.

Draft tube sensor DT1, DT2 and DT3 display the guide vane frequency at 27.78 with 4.8e-08, 6.42e-08 and 6.03e-07 respectively.

5.1.6 Generator Torque

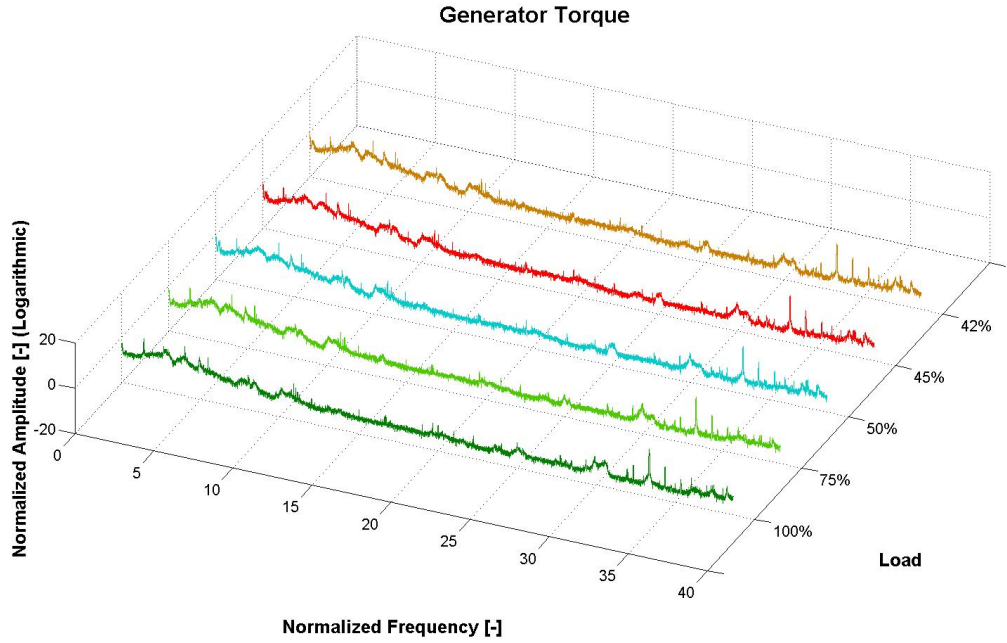


Figure 5.6: Frequency domain of the generator torque at various loads

There are peaks present at approximately 1.3, 4, 17, 30, 33 and 34 on the x-axis. The Norm. amplitudes are presented in Table 5.17.

Norm. Frequency [-]	100% load	75% load	50% load	45%	42% load
1.34	20.99	6.75	0.91	1.12	0.068
4	69.18	81.28	114.29	30.55	67.76
16.66	2.13e-10	1.96e-10	1.29e-10	1.05e-10	3.16e-11
29.97	1.43e-08	1.59e-07	9.82e-08	5.45e-08	7.46e-09
33.32	5.89	13.9	7.94	5.5	9.12
33.34	3.12e-06	4.63e-06	3.54e-05	3.77e-05	1.15e-04

Table 5.17: Norm. Amplitudes of Generator Torque frequency at various operating conditions.

5.1.7 Draft tube

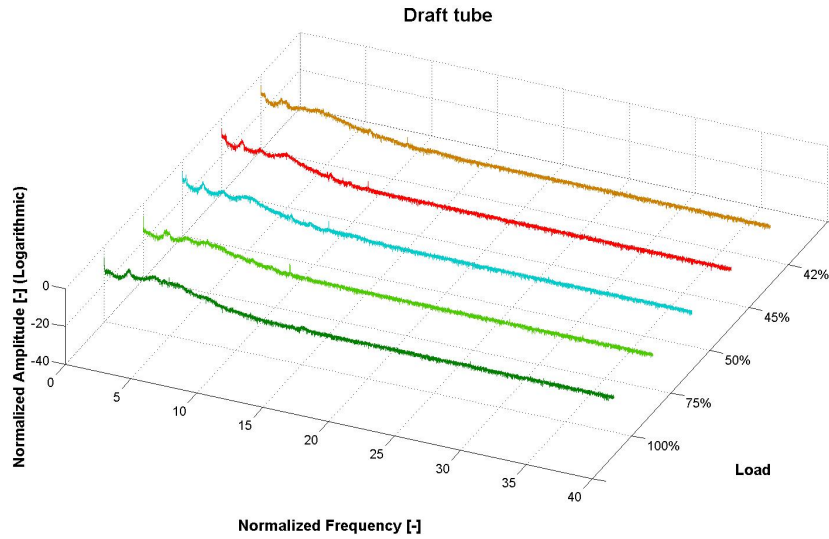


Figure 5.7: Frequency domain of draft tube sensor at various loads

There are small peaks visible at 1.5 and 11 on the x-axis. The Norm. amplitudes are presented in Table 5.18.

Norm. Frequency [-]	100% load	75% load	50% load	45%	42% load
1.51	5.33e-10	1.1e-12	1.47e-09	8.79e-10	8.13e-11
11.11	1.95e-19	2.88e-16	2.75e-16	8.13e-18	6.03e-17

Table 5.18: Norm. Amplitudes of draft tube frequency at various operating conditions.

5.1.8 Low frequency regime

The lower frequency domains of runner sensors, generator torque and draft tube cone sensors are presented. The low frequencies are of interest with respect to locating the Rhengans frequency and possible detachments through the runner. There are no clear peaks in the lower frequency domains at 100% and 75% load. These figures are therefore not included in this section but are available in Appendix E. The runner frequency is visible in these figures but have been treated earlier and is therefore not included in the tables.

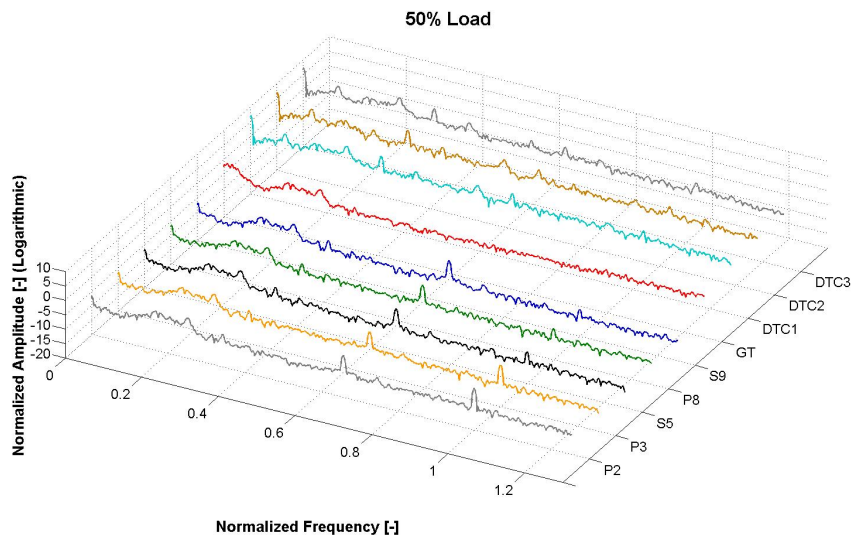


Figure 5.8: Low frequency regime of runner sensors, generator torque and draft tube cone at 50% load

Peaks are visible around 0.25, 0.34, 0.6 and 0.66 on the x-axis. The norm. amplitudes are presented in Table 5.19. The draft tube cone sensors displays very high amplitudes at low loads. The reason for this behaviour and its effect on the results will be discussed in a later chapter.

Sensor	Norm. Amplitude [-] at 0.253	Norm. Amplitude [-] at 0.342	Norm. Amplitude [-] at 0.5961	Norm. Amplitude [-] at 0.658
P2	8.43e-07	4.8e-06	-	3.42e-06
P3	1.26e-06	2.33e-09	-	3.66e-06
S5	1.74e-06	2.71e-09	-	2.82e-06
P8	1.04e-06	2.36e-09	-	2.88e-06
S9	8.65e-07	2.81e-09	-	7.18e-06
Generator	7.06e-03	2.51e-09	-	-
DTC1	63241	36728	92.68	533
DTC2	222	141579	2811	770
DTC3	169824	20653	375	362

Table 5.19: Norm. Amplitudes of the lower frequency regime in sensors at 50% Load

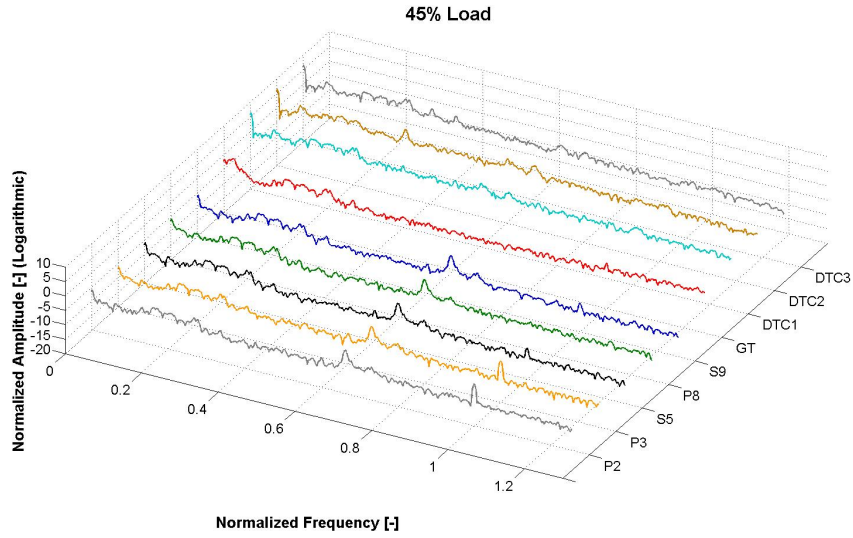


Figure 5.9: Low frequency regime of runner sensors, generator torque and draft tube cone at 45% load

Peaks are visible around 0.27 and 0.66 on the x-axis. The norm. amplitudes are presented in Table 5.20.

Sensor	Norm. Amplitude [-] at 0.27	Norm. Amplitude [-] at 0.66
P2	1.31e-07	9.27e-06
P3	1.01e-07	1.26e-05
S5	9.14e-08	9.98e-06
P8	1.64e-07	1.16e-05
S9	1.15e-07	1.77e-05
Generator	5.14e-04	-
DTC1	1710	16.2
DTC2	5.48	173
DTC3	5714	15.14

Table 5.20: Norm. Amplitudes of the lower frequency regime in sensors at 45% Load

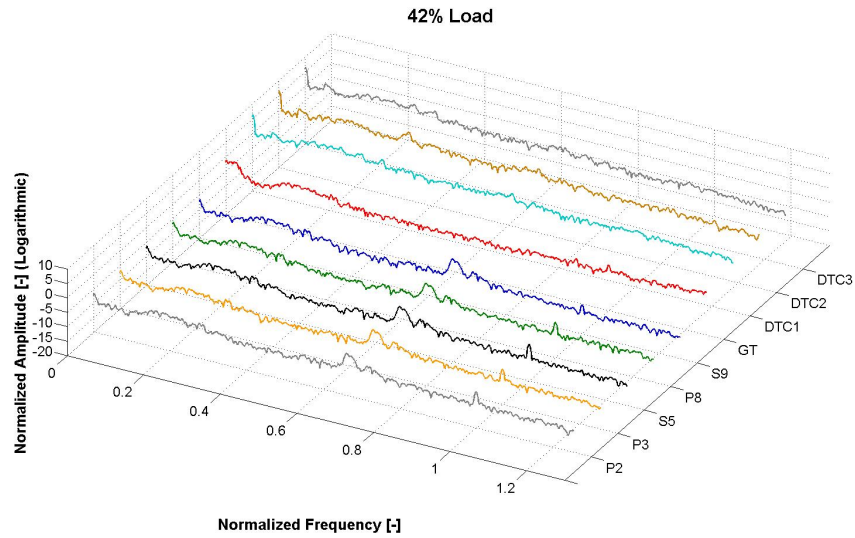


Figure 5.10: Low frequency regime of runner sensors, generator torque and draft tube cone at 42% load

Peaks are visible around 0.28 and 0.66 on the x-axis. The norm. amplitudes are presented in Table 5.21.

Sensor	Norm. Amplitude [-] at 0.28	Norm. Amplitude [-] at 0.66
P2	1.33e-08	3.72e-06
P3	1.64e-08	4e-06
S5	1.5e-08	2.7e-06
P8	1.06e-08	2.4e-06
S9	1.27e-08	5.2e-06
Generator	7.24e-05	-
DTC1	180	40
DTC2	3.38	129
DTC3	1238	13.3

Table 5.21: Norm. Amplitudes of the lower frequency regime in sensors at 42% Load

5.2 Phase averaged

This section contains plot of the angularly resolved phase averaged data for stationary and rotating sensors. 360 degrees has been divided into 720 bins and data has been averaged and divided into these bins. The shifted phase of sensor P23, P33 and P34 is due to their geometrical position in the vaneless space. The phase is not aligned for visual purposes, as the lines become difficult to observe when the phases are aligned. Due to time limitation of this project, only draft tube cone sensor DTC2 was chosen for phase averaging. An example of phase averaging of sensor P2 plotted with raw data can be found in Appendix F.

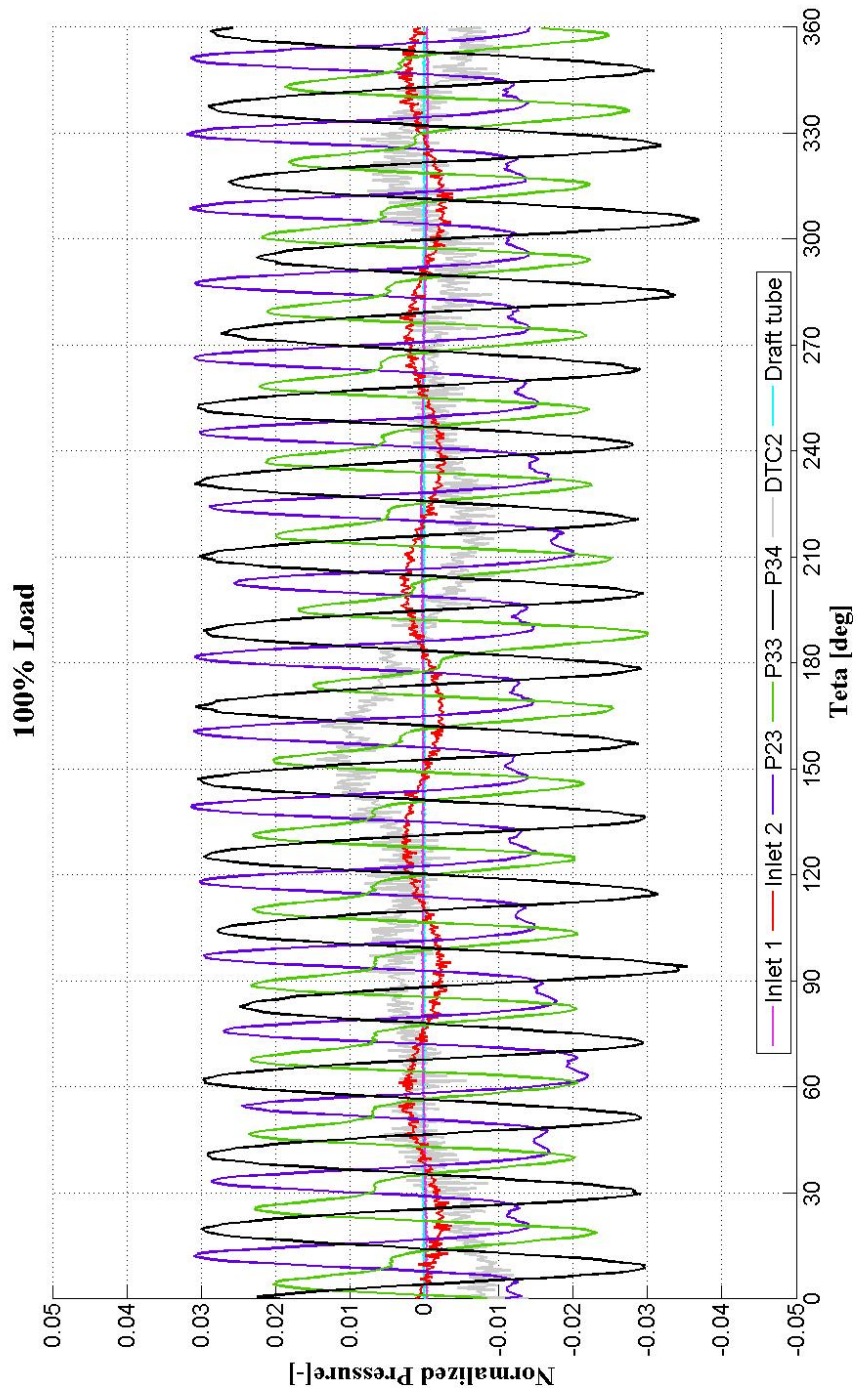


Figure 5.11: Angularly resolved data from stationary sensors at 100% load

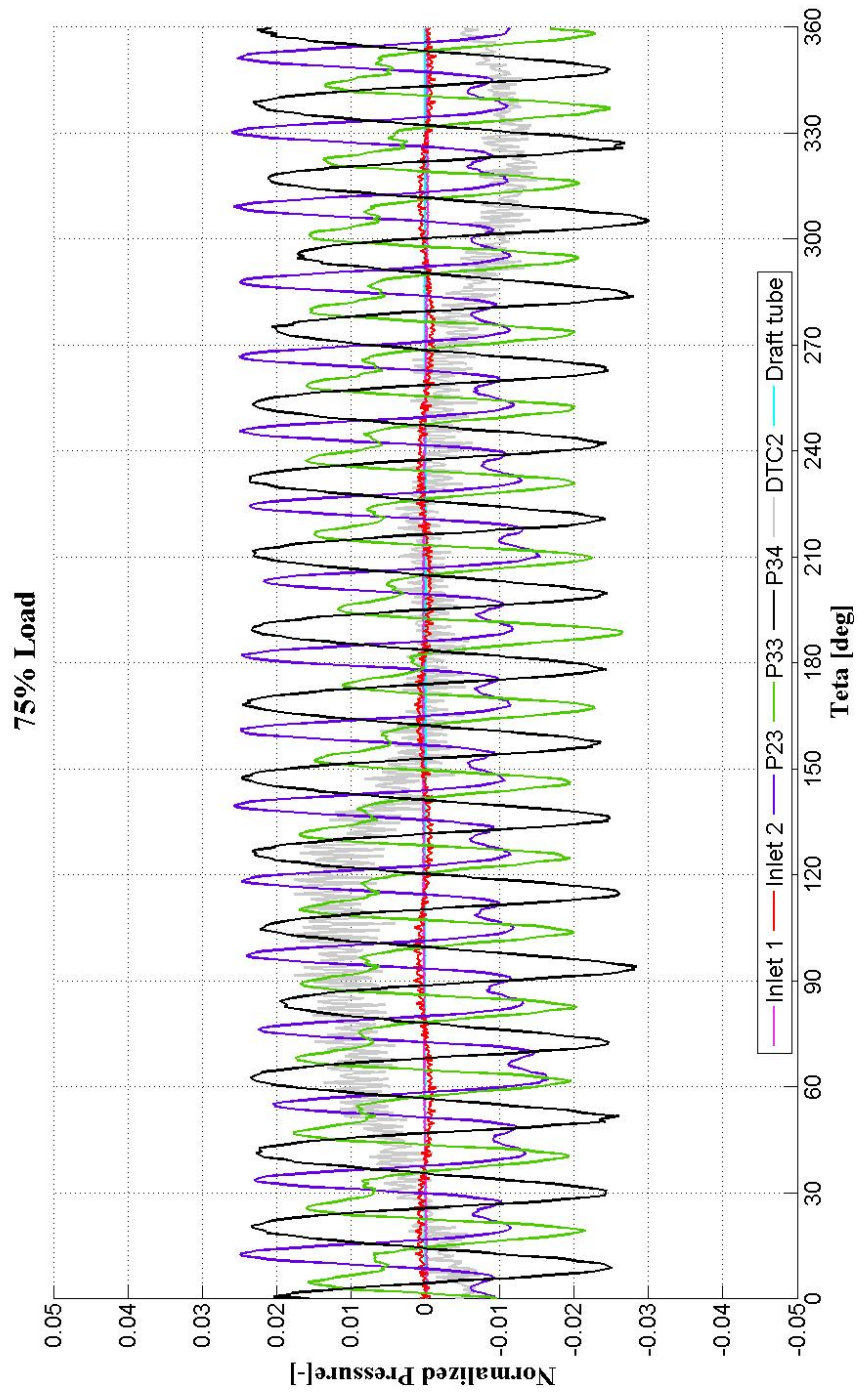


Figure 5.12: Angularly resolved data from stationary sensors at 75% load

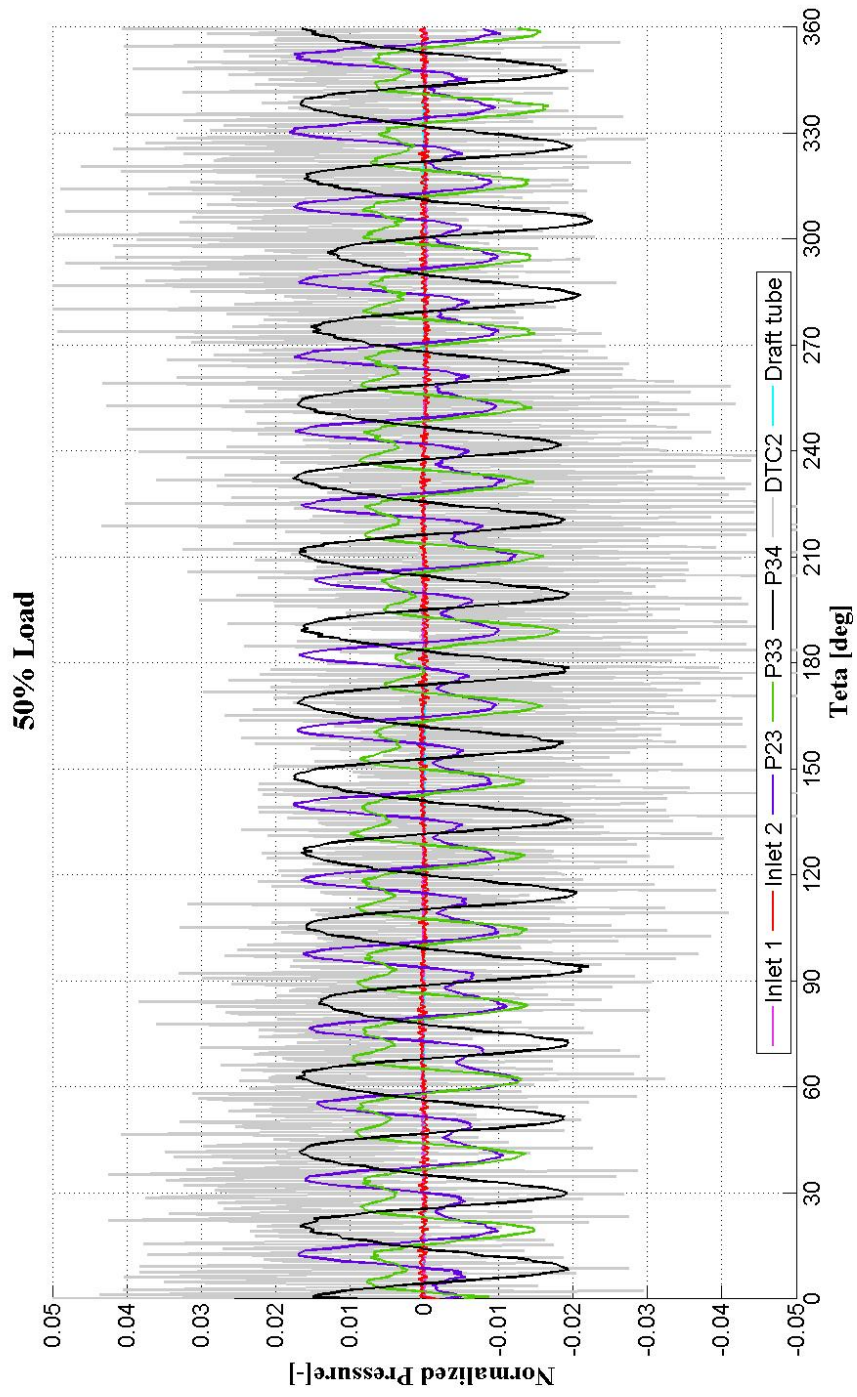


Figure 5.13: Angularly resolved data from stationary sensors at 50% load

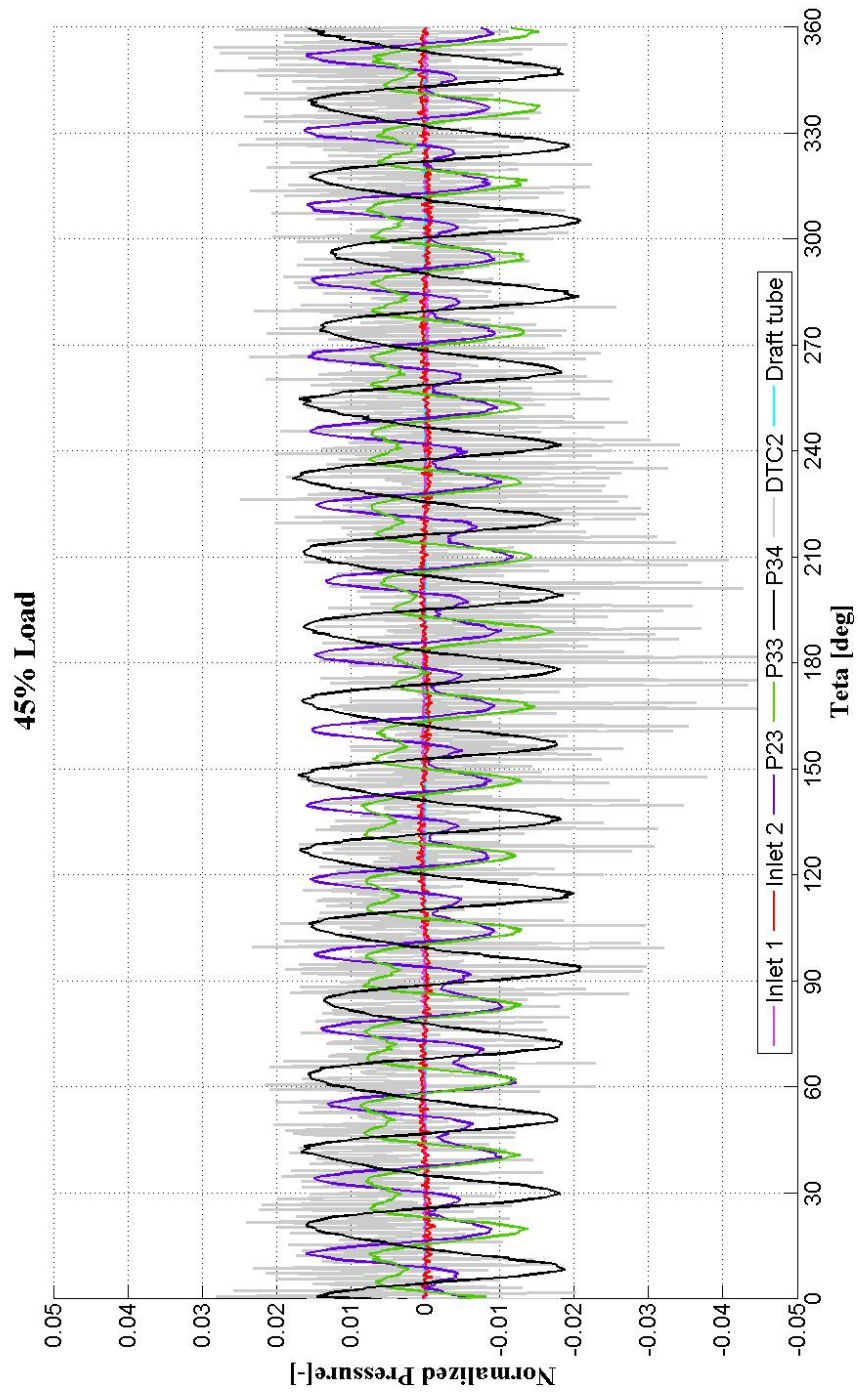


Figure 5.14: Angularly resolved data from stationary sensors at 45% load

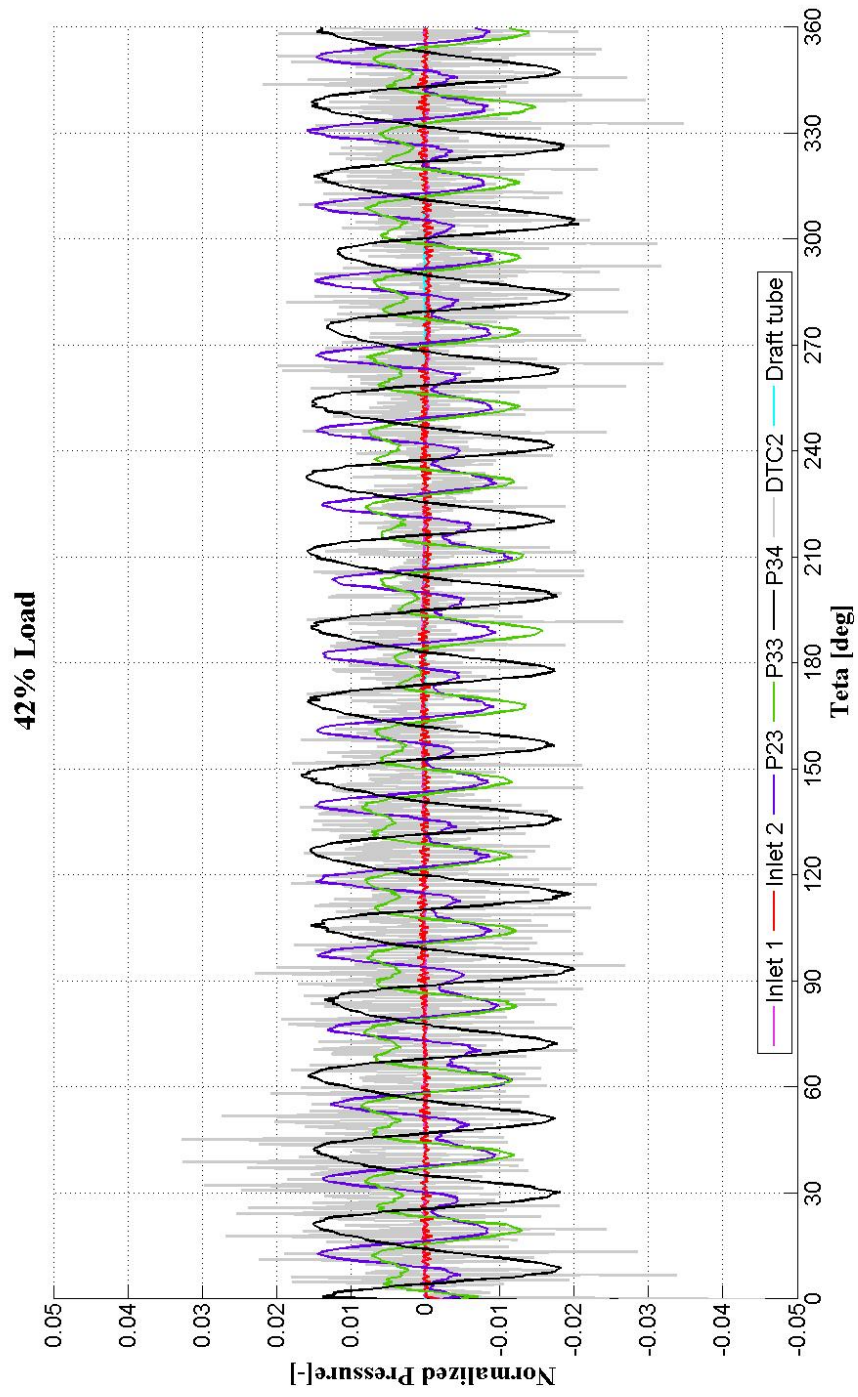


Figure 5.15: Angularly resolved data from stationary sensors at 42% load

5.2.1 Stationary sensors

Notice dips in the phase of sensor P33 and P23 in Figures 5.14 and 5.15. Sensor P34 does not display this behaviour, indicating that this is most likely a physical phenomena rather than a product of the signal processing. This subject will be explained in detail later.

At 100% load the RSI pulsations are dominating the high amplitudes (see Figure 5.11). Inlet 2 transducer is oscillating at a rate that corresponds to the elastic fluctuation mentioned in Section 5.1. There are no clear correlations between the phase of the vaneless space transducers and in the draft tube.

Figure 5.12 displays the phase averaged data for stationary sensors at 75% load. The amplitudes of the inlet sensor are dampened and the fluctuations in the draft tube cone are widened and appear to have a more uniform distribution. This could indicate formation of a vortex in the draft tube.

Figure 5.13 displays the phase averaged data for stationary sensors at 50% load. The RSI pulsations are now clearly dampened. The phase of the vaneless space transducers have more rounded tops, but the irregularities are still visible in sensor P23 and P33. There are no clear signs of impact from the draft tube of vaneless space on the inlet sensors. The amplitudes in the draft tube cone have increased considerably, indicating a strong vortex. If we have a closer look at the phases of sensor P33 and the draft tube cone sensor, there appears to be signs of correlation. Figure 4.5 confirms that sensor P33 and sensor DTC2 are positioned in the same radial section on the rig.

Figure 5.14 displays the phase averaged data for stationary sensors at 45% load. Both the draft tube and the RSI pulsations are now decreasing. A correlation between P33 and DTC2 is still apparent.

Figure 5.14 displays the phase averaged data for stationary sensors at 42% load. All pulsations are now dampened, but the correlation between P33 and DTC2 is still apparent.

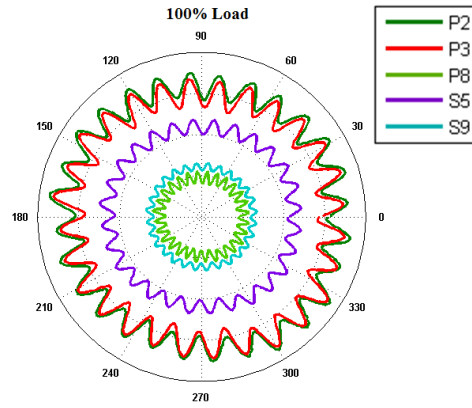


Figure 5.16: Angularly resolved data of rotating sensors at 100% load

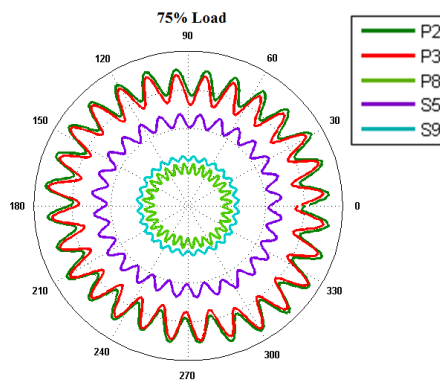


Figure 5.17: Angularly resolved data of rotating sensors at 75% load

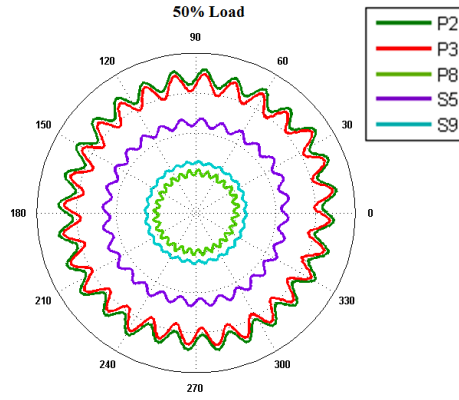


Figure 5.18: Angularly resolved data of rotating sensors at 50% load

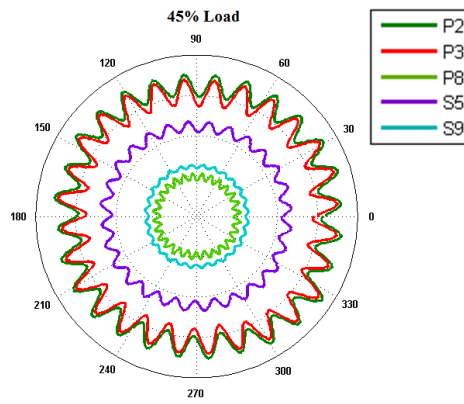


Figure 5.19: Angularly resolved data of rotating sensors at 45% load

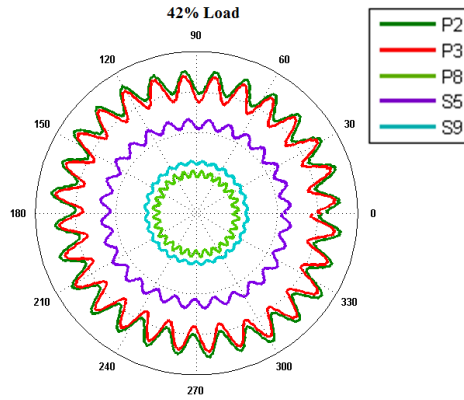


Figure 5.20: Angularly resolved data of rotating sensors at 42% load

5.2.2 Rotating sensors

Figures 5.16, 5.17, 5.18, 5.19 and 5.20 displays the phase averaged data of the rotating sensors at 100%, 75%, 50%, 45% and 42%, respectively. The pulsations are strongest at sensors P2 and P3 in section 1. The oscillations are dampened through the runner and appears to be weaker at the outlet in sensor P8. The pulsations also appear to be weaker on the pressure side, with more rounded shapes of the phase peaks.

At 100% and 75% load the phases appear similar. At 50% the peaks in the phases become more rounded, this is particularly clear on the pressure side sensors. At 45% load the signal appears to be slightly amplified with more predominant peaks. This can indicate that the strong vortex present at 50% load affects the phase properties of the runner sensors. At 42% load the phases of the pressure sensors has flattened out further. The averaged phases of the sensors on the pressure side appears unchanged.

The 4.9 frequency appears to be flow independent and is probably what Tørklep found during his spectral analysis on data from a different turbine in the rig. However, it seems like 4.9 is the predominant frequency and not the half harmonic as Tørklep concluded.

The peaks at 11, 32 and 32 appear to have a structural origin as they are not flow dependent. They have their highest amplitudes in the draft tube cone and in the generator torque. This is likely to be a structural oscillation that starts in the generator and moves down through the draft tube under the rig.

The peak at 1.34 in the frequency domain of the generator seems to be flow dependent and reduces significantly as the load is decreased. This frequency is also apparent as small peaks in the domain of runner sensors P2, P3 and S5. Existence of pulsations in rotating channels and generator torque is most likely due to some form of mass oscillation through the runner. The source of this mass oscillation has not been located.

The peaks at 1.51 in the draft tube outlet does not appear to be flow dependent and are assumed to be caused by structural vibrations in the low pressure parts of the system.

Peaks at 0.66 appear when the load is reduced to 50%. This frequency is independent of flow. It is therefore thought that it can originate from structural oscillations that interfere with the draft tube vortex. During testing, vibrations were noticeable at loads lower than 75%. It is likely that this frequency can be connected to these vibrations, but this has not been successfully confirmed at this stage.

Peaks at 0.34 and 0.6 were detected at 50% load. These frequencies were not observed under any other operating conditions. The situation in the draft

tube was very chaotic at this operating point, with a large, unstable vortex. In addition, air was leaking into the system and the effects of this leakage on the frequency domain is not known. These frequencies are therefore suspected to be products of the chaotic situation in the draft tube at the present operating condition.

6.1 Runner frequency

Figure 6.1 displays the normalized amplitudes of the runner frequency in logarithmic scale.

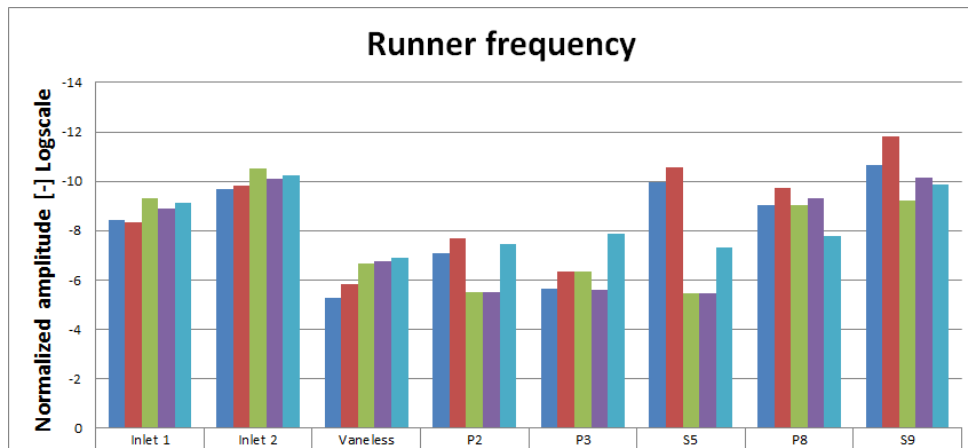


Figure 6.1: Normalized amplitudes of runner frequency at various loads

The frequency appears to be flow dependent in the inlet sensors and the vaneless space. The larger amplitudes are found in the vaneless space and in sensors P2 and P3 on the blade, closest to the trailing edge.

6.2 RSI

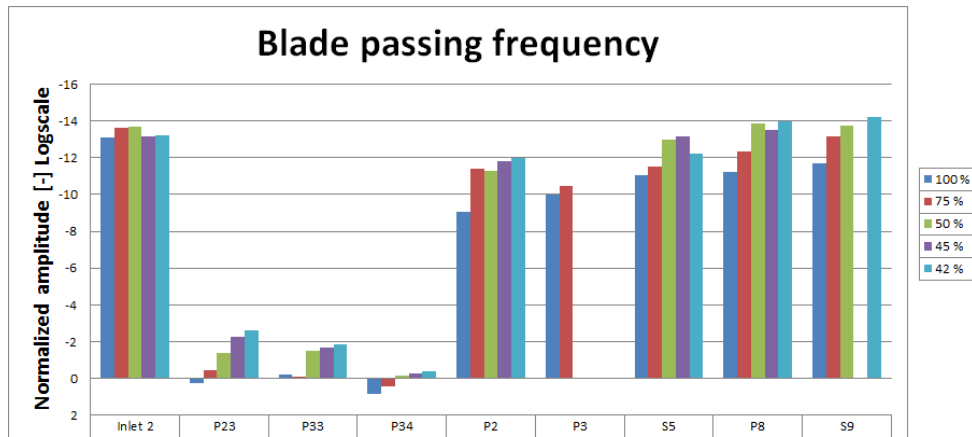


Figure 6.2: Normalized amplitudes of the blade passing frequency at various loads

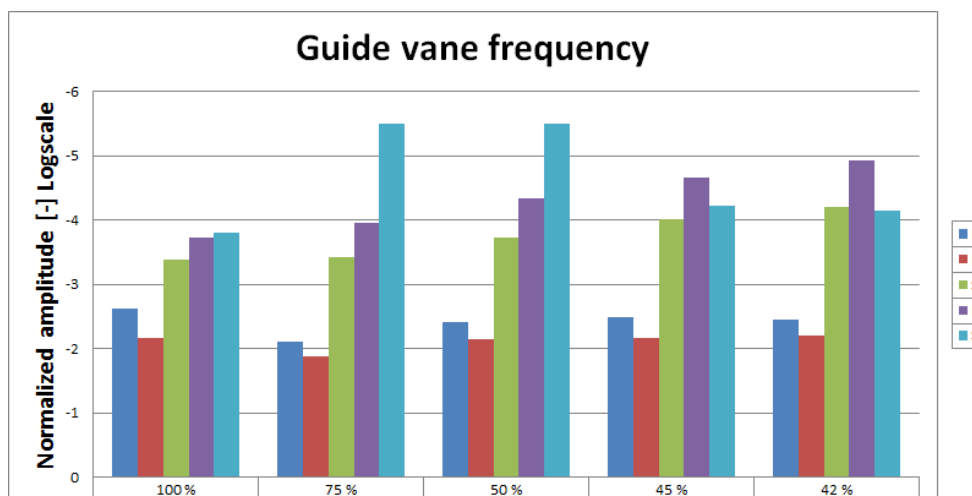


Figure 6.3: Normalized amplitudes of the guide vane frequency at various loads

Figure 6.2 display the pulsations in the vaneless space. It is apparent that the amplitudes of the blade passing frequency is flow dependent. This is according to Bernoulli which states that pressure decreases with increasing velocity. Further, we can observe from Figure 6.2 and Figure 6.3 that pulsations are dampened through the runner. This can be a result of the mixing phenomena that occurs at the end of the blade when the pressure and suction parts of the channel flow interacts.

Kobro has done a similar experiment during his work at NTNU. Tests were performed on the same rig, with a split blade turbine. Kobro discussed whether the split blades amplifies dampening of RSI induced pulsations due to increased mixing of the pressure fields at the outlet of the split blade [Kobro, 2012]. In his work the amplitudes from inlet to outlet of the runner were dampened by approximately 86% at BEP. Results presented in this thesis indicate a dampening of approximately 92.3% at BEP from sensor P2 to sensor P8 along the same streamline. However, this result is associated with many uncertainties. The few number of sensors and only one dataseries does not allow for statistical comparison. Thus, this is only an indication that the full blade model dampens the pulsations as efficient as the spilt blade turbine.

Kobro also did a comparison of the pulsations in the vaneless space with varying load. His results indicated a decrease in relative amplitude of approximately 24% from 100% to 50% load. The results obtained in this work shows a reduction in relative amplitude of approximately 92.1% from the same load variation. This significant difference can be explained by variables such as blade angle, number of blades and runner speed. However, the difference is substantial and should be investigated further. In relation to this it should be stressed that model turbines of different geometries are not directly comparable to each other. Therefore, the comparison with Kobros data is not directly relevant for the results in this project.

6.3 Rheingans Frequency

Due to an air leakage in the shaft (See Appendix D) there is a lot of noise apparent on the draft tube cone transducers. Hence, there are several peaks in the frequency domain, complicating the mapping of the expected frequencies of the system. The unsteady movements of contained air interferes with the stochastic behaviour of the flow in the draft tube and introduces large uncertainties to the analysis.

The draft tube sensors display very high peaks at low frequencies. This could be due to properties of the sensors, and the amplitudes of the draft tube sensors at low load are interpreted with some scepticism. Unfortunately, due to time limitations, this has not been investigated further.

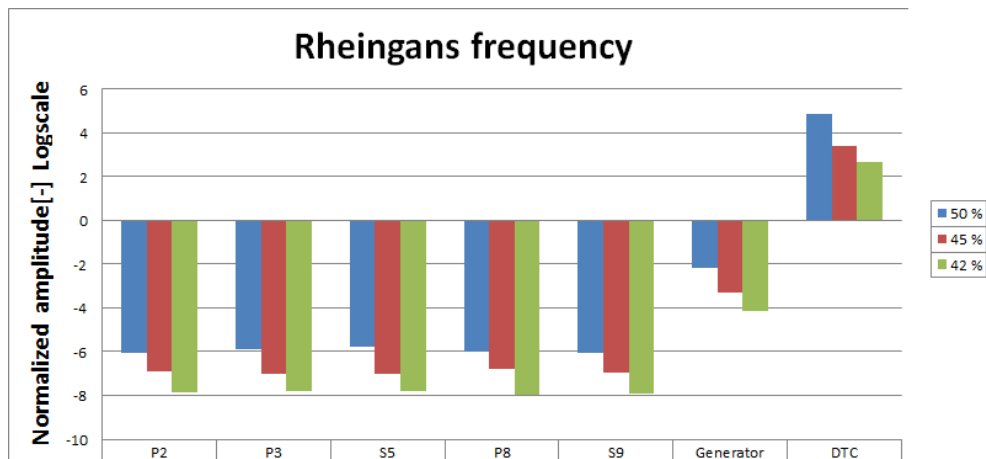


Figure 6.4: Normalized amplitude of the Rheingans frequency at 50%, 45% and 42% load

Figure 6.4 displays the relative amplitude of the Rheingans frequency in the draft tube cone at 50%, 45% and 42% load. The frequency is clearly flow dependent and propagates upwards through the runner. There is not a clear distribution of the amplitudes over the runner sections as one might have expected. This is also apparent in Kobros results [Kobro, 2012]. Kobro discussed the possibility of mass flow fluctuation through the runner, due to the low frequent nature of the draft tube pulsations. From Figure 6.4 the Rheingans frequency is present in the generator torque which indicates that the low frequent pulsations causes mass fluctuations through the runner and influences the power output of the generator.

6.4 Spiral casing

Figure 5.11 and 5.15 in section 5.2.1 displayed irregularities in the signal from vaneless space transducers P23 and P33. This can indicate a disturbance between the two sensors in the spiral casing. One explanation can be that asymmetry in the spiral casing, the so called heart valve, causes two of the sensors to experience these irregularities (See Figure 4.5). Another explanation can be what former Master student at the waterpower laboratory, Andrea Stranna [Stranna, 2013] experienced during her work. Stranna discovered irregularities while running a turbine in pump mode and concluded that one or several guide vanes were oscillating at certain operating points.

An asymmetry in the spiral casing will be visible in the rotating pressure sensors at the trailing edge. The angularly resolved Figures 5.20 and 5.16 does not indicate any apparent disturbances in the spiral casing. The raw data from 2 rotations of the runner sensors are plotted as high gradients can be filtered out in the mean phase figures. Several rotations were looked at to check for consistency of this irregularity. Only two rotations are plotted for visual purposes.

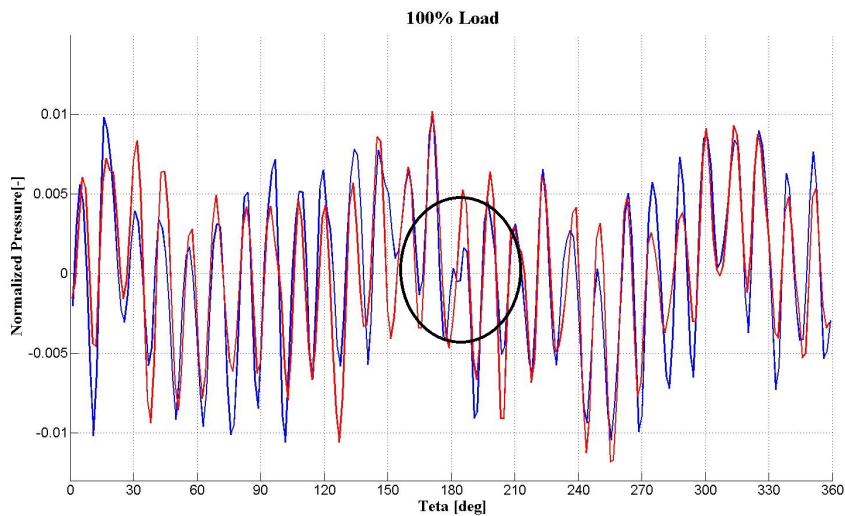


Figure 6.5: 2 rotations resolved angularly, Sensor P2

Figure 6.5 presents two rotations of a blade sensor close to the trailing edge. From 150-210 deg there are irregularities in the signal and a dip at approximately 180 deg is circled in. According to Figure 4.5 the assumed asymmetry in the spiral casing would be situated approximately 200-250 degrees from the keyphasor reference point. This would correspond to 155-205 deg rotation of

the blade sensors. It is therefore likely that the disturbances in the spiral casing originate from an area close to the heart valve.

6.5 Data acquisition system

One of the objectives of this thesis was to achieve simultaneous measurements with two separate logging units. The logging system proved to be successful. By using the triggerfunction on the compact RIOs the sampling was started within microseconds, and any deviation could be corrected by using the signal from a keyphasor to align the sampled data. There were some problems with the triggerfunction to begin with. Noise on the triggersignal caused the cRIOs to trig uncontrollably and files were created every 45-60 seconds. This problem was bypassed by introducing a time-delay in the Labview program so that the triggersignal had to be sustained for 500 ms for the cRIOs to start sampling (LabVIEW program can be found in digital Appendix).

The cRIO setup proved to be very efficient for precise sampling of large amount of data, however the system was unreliable at times. Several sampling series were interrupted during the experiments. The reason for this is not known but it is possible that the G-forces exerted on the rotating RIO causes it to fail occasionally.

Several frequencies has been observed at the different operating conditions. In addition to the runner frequency (1), blade passing frequency (17) and guide vane passing frequency (28), peaks at approximately 1.34, 4.9, 11, 32 and 33 has been observed. In the low frequency regime, the Rheingans frequency (2.5-2.7) is clearly present from 50% load. Peaks at 0.34, 0.6 and 0.66 is also observed in the low frequency regime.

4.9 is not flow dependent and is recognized as an elastic fluctuation in the system. 11, 32, 33 and 0.66 are independent on flow and are assumed to have structural origins. 0.34 and 0.6 appear at low loads when there is a strong vortex in the draft tube. They are not dependent on flow and are assumed to be caused by stochastic phenomenas in the draft tube. 1.34 was apparent in the generator torque and the rotating sensors and seems to be flow dependent. It is asumed to have the form of mass oscillation through the runner, but its origin is not known at this stage.

The blade passing frequency is predominant in the vaneless space. An irregularity is observed on 2 vaneless space sensors. It is assumed that this is caused by asymmetric properties of the spiral casing geometry.

The guide vane frequency dominates in the runner channels and RSI-induced pulsations are dampened through the runner due to mixing of pressure fields. Results show that pressure pulsations are weaker on the suction side of the blade. However, due to the low number of sensors remaining this is associated with high uncertainties. RSI-induced pulsations decrease as the flow is reduced.

Rheingans frequency is observed in the runner channels and the generator torque which indicates mass oscillations through the system.

Analysis and comparison of pressure pulsations and stresses was not conducted as the installed strain gauges were defect.

The experimental setup allowed for simultaneous sampling with two units but the compact RIOs were unreliable in operation.

CHAPTER 8

FURTHER WORK

Replace O-ring on the rig to seal air leakage through the shaft.

Add a wireless router to the rotating cRIO in order to transfer data during sampling. This would make it possible to monitor both cRIOs during experiments and transfer data so that the memory does not overflow when sampling long timeseries.

Replace the defect sensors and strain gages in the runner and create a waterproof seal around the socket so that water is not able to penetrate.

Construct a new calibration tank that can be filled with air. The measuring equipment can then be placed inside the tank and waterleakage through the wire outlet would be avoided.

Perform extensive testing on the model turbine. The whole operating range should be sampled in order to map out more accurately the amplitudes and frequencies that arises in the system. Several independent measurements should be done in order to permit statistical evaluation. The triggersignal of the cRIO should also be connected to a high speed camera in order to have simultaneous visual data in addition to pressure measurements.

Investigate the effects of the heart valve in the spiral casing in relation to the RSI pulsations.

Do an investigation on the piezoelectric sensors in the draft tube cone. Find out why they display such high amplitudes at low frequencies and how this affects the test results.

Map out the stresses on the runner blades on a wide range of operating conditions.

REFERENCES

- [Arndt, 1990] Arndt, R. E. (1990). Hydraulic turbines. *Energy*, 2:2.
- [Cervantes et al., 2008] Cervantes, M., Jansson, I., Jourak, A., Glavatskih, S., and Aidanpää, J.-O. (2008). Porjus U9A full-scale hydropower research facility. In *Hydro technology and the environment for the new century: 24th IAHR Symposium on Hydraulic Machinery and Systems*.
- [Ciocan et al., 2007] Ciocan, G. D., Iliescu, M. S., Vu, T. C., Nennemann, B., and Avellan, F. (2007). Experimental study and numerical simulation of the FLINDT draft tube rotating vortex. *Journal of Fluids Engineering*, 129(2).
- [Dorfler et al., 2013] Dorfler, P., Sick, M., and Coutu, A. (2013). Periodic effects of runner-casing interaction. In *Flow-Induced Pulsation and Vibration in Hydroelectric Machinery*, pages 69–110. Springer.
- [Frunzâverde et al., 2010] Frunzâverde, D., Muntean, S., Mârginean, G., Câmpian, V., Marşavina, L., Terzi, R., and Şerban, V. (2010). Failure analysis of a francis turbine runner. *IOP Conference Series: Earth and Environmental Science*, 12(1).
- [Haugan, 2012] Haugan, K. (2012). Trykkpulsasjoner i francisturbiner.
- [Heinzel et al., 2002] Heinzel, G., Rüdiger, A., Schilling, R., and Hannover, T. (2002). Spectrum and spectral density estimation by the discrete fourier transform (DFT), including a comprehensive list of window functions and some new flat-top windows. *Max Plank Institute*, 12:122.
- [Instruments, 2013a] Instruments, N. (2013a). Developing custom measurement and control i/o hardware with the labview fpga module and reconfigurable i/o hardware.
- [Instruments, 2013b] Instruments, N. (2013b). Ni product manuals.
- [Kobro, 2012] Kobro, E. (2012). *Measurement of Pressure Pulsations in Francis Turbines*. PhD thesis.

- [Mathworks, 2013] Mathworks (2013). filtering and smoothing data.
- [Nielsen, 1990] Nielsen, T. K. (1990). *Dynamisk dimensjonering av vannkraftverk*. SINTEF, Strømningsmaskiner.
- [Rheingans, 1940] Rheingans, W. J. (1940). Power swings in hydroelectric power plants. *Trans. ASME*, 62:171–184.
- [Ruprecht et al., 2002] Ruprecht, A., Helmrich, T., Aschenbrenner, T., and Scherer, T. (2002). Simulation of vortex rope in a turbine draft tube. In *Proceedings of the 21st IAHR Symposium on Hydraulic machinery and systems, Lausanne, Switzerland*.
- [Seidel et al., 2012] Seidel, U., Hübner, B., Löfflad, J., and Faigle, P. (2012). Evaluation of RSI-induced stresses in francis runners. *IOP Conference Series: Earth and Environmental Science*, 15(5):052010.
- [SENOO et al., 1978] SENOO, Y., KAWAGUCHI, N., and NAGATA, T. (1978). Swirl flow in conical diffusers. *Bulletin of JSME*, 21(151).
- [Sonnenberger et al., 2000] Sonnenberger, R., Graichen, K., and Erk, P. (2000). Fourier averaging: a phase-averaging method for periodic flow. *Experiments in Fluids*, 28(3):217–224.
- [Storli, 2006] Storli, P. T. (2006). Modelltest av francis turbin i vannkraftlaboratoriet.
- [Stranna, 2013] Stranna, A. (2013). Testing of rpt in pumping mode of operation.
- [Tørklep, 2012] Tørklep, A. M. (2012). Pressure oscillations during start and stop of a high head francis turbine.
- [Thomas Zawistowski, 2013] Thomas Zawistowski, P. S. (2013). An introduction to sampling theory.
- [Trivedi et al., 2013] Trivedi, C., Gandhi, B., and Michel, C. J. (2013). Effect of transients on francis turbine runner life: a review. *Journal of Hydraulic Research*, 51(2):121–132.
- [Wheeler, 2004] Wheeler, A. J. (2004). *Introduction to Engineering Experimentation (2nd Edition)*. Prentice Hall, Upper Saddle River. New Jersey.

APPENDIX

- Appendix A - Calibration reports
- Appendix B - Runner Sensors
- Appendix C - Rig setup
- Appendix D - Air leakage
- Appendix E - cRIO Installation
- Appendix F - Results
- Appendix G - Risk assesment

All MATLAB scripts and Labview programs can be found in the electronic appendix.

Appendix A - Calibration

This section contains calibration documents of equipment used prior to and during experiments.

CALIBRATION REPORT

CALIBRATION PROPERTIES

Calibrated by: Julie Marie Hovland, Ingeborg Lassen Bue
Type/Producer: Kulite XTE-190
SN: v4537-23
Range: 0-3.5 bar a
Unit: kPa

CALIBRATION SOURCE PROPERTIES

Type/Producer: Pressurements deadweight tester P3223-1
SN: 66256
Uncertainty [%]: 0,01

POLY FIT EQUATION:

$Y = + 13.46620876E+0X^0 + 70.31068838E+3X^1$

CALIBRATION SUMMARY:

Max Uncertainty : 0.026225 [%]
Max Uncertainty : 0.026147 [kPa]
RSQ : 1.000000
Calibration points : 19

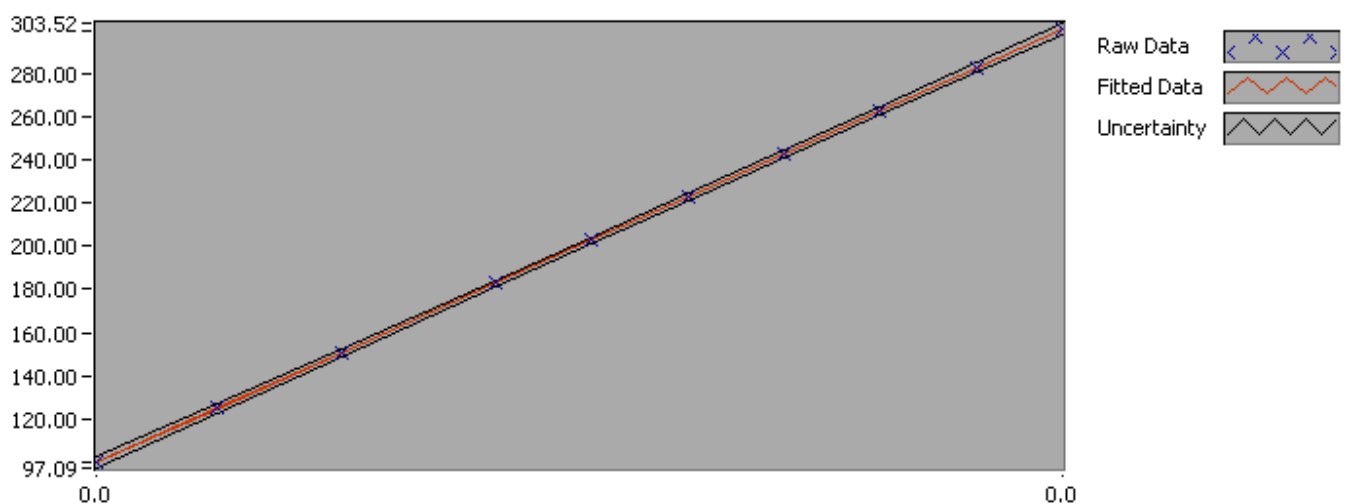


Figure 1 : Calibration chart (The uncertainty band is multiplied by 100)

Value [kPa]	Voltage [V]	Best Poly Fit [kPa]	Deviation [kPa]	Uncertainty [%]	Uncertainty [kPa]
99.700000	0.001227	99.744861	-0.044861	0.026225	0.026147
124.737768	0.001582	124.706393	0.031375	0.017380	0.021679
150.777046	0.001953	150.748387	0.028659	0.011675	0.017603
182.825389	0.002409	182.830970	-0.005581	0.007765	0.014196
202.855603	0.002694	202.893936	-0.038333	0.006675	0.013540
222.885817	0.002979	222.903882	-0.018065	0.006396	0.014256
242.916031	0.003264	242.936142	-0.020110	0.006654	0.016164
262.946246	0.003548	262.960679	-0.014434	0.007186	0.018894
282.976460	0.003833	282.978510	-0.002050	0.007831	0.022160
301.003653	0.004089	300.980524	0.023128	0.008431	0.025377
282.976460	0.003833	282.963856	0.012604	0.007831	0.022160
262.946246	0.003548	262.947648	-0.001403	0.007186	0.018894
242.916031	0.003263	242.920165	-0.004133	0.006650	0.016155
222.885817	0.002978	222.883488	0.002329	0.006394	0.014252
202.855603	0.002693	202.845802	0.009802	0.006675	0.013540
182.825389	0.002409	182.809547	0.015842	0.007765	0.014196
150.777046	0.001953	150.760591	0.016456	0.011675	0.017603
124.737768	0.001582	124.721234	0.016533	0.017380	0.021679
99.700000	0.001227	99.707757	-0.007757	0.026225	0.026147

Julie Marie Hovland, Ingeborg Lassen Bue

The uncertainty is calculated with 95% confidence. The uncertainty includes the randomness in the calibrated instrument during the calibration, systematic uncertainty in the instrument or property which the instrument under calibration is compared with (dead weight manometer, calibrated weights etc.), and due to regression analysis to fit the calibration points to a linear calibration equation. The calculated uncertainty can be used as the total systematic uncertainty of the calibrated instrument with the given calibration equation.

CALIBRATION REPORT

CALIBRATION PROPERTIES

Calibrated by: Julie Marie Hovland, Ingeborg Lassen Bue
Type/Producer: Kulite XTE-190
SN: v4537-33
Range: 0-7 bar a
Unit: kPa

CALIBRATION SOURCE PROPERTIES

Type/Producer: Pressurements deadweight tester P3223-1
SN: 66256
Uncertainty [%]: 0,01

POLY FIT EQUATION:

$Y = + 54.48242625E+0X^0 + 154.91703928E+3X^1$

CALIBRATION SUMMARY:

Max Uncertainty : 0.073561 [%]
Max Uncertainty : 0.073340 [kPa]
RSQ : 0.999998
Calibration points : 20

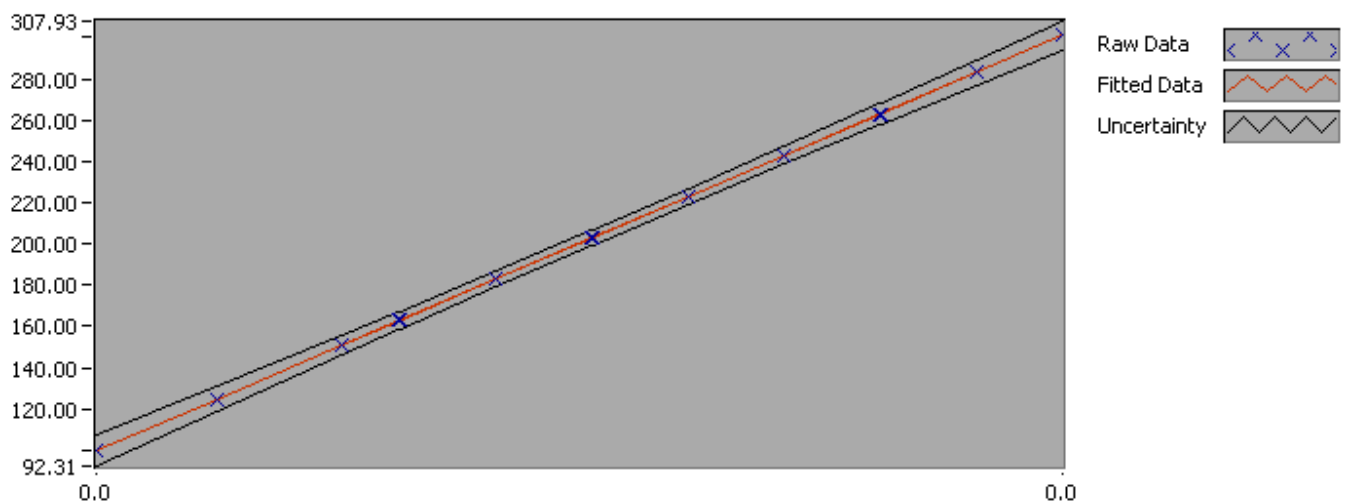


Figure 1 : Calibration chart (The uncertainty band is multiplied by 100)

Value [kPa]	Voltage [V]	Best Poly Fit [kPa]	Deviation [kPa]	Uncertainty [%]	Uncertainty [kPa]
99.700000	0.000292	99.643086	0.056914	0.073561	0.073340
124.737768	0.000453	124.605899	0.131869	0.048354	0.060316
150.777046	0.000621	150.710487	0.066559	0.031999	0.048248
162.795175	0.000699	162.718022	0.077153	0.026743	0.043536
182.825389	0.000828	182.753607	0.071782	0.020647	0.037748
202.855603	0.000957	202.792384	0.063219	0.017492	0.035484
222.885817	0.001087	222.824113	0.061705	0.016790	0.037423
242.916031	0.001216	242.863519	0.052512	0.017691	0.042974
262.946246	0.001345	262.896836	0.049410	0.019384	0.050970
282.976460	0.001475	282.914685	0.061775	0.021389	0.060525
301.003653	0.001591	300.944070	0.059583	0.023197	0.069823
282.976460	0.001475	282.981097	-0.004637	0.021388	0.060524
262.946246	0.001346	263.011964	-0.065718	0.019410	0.051038
242.916031	0.001217	243.019369	-0.103338	0.017713	0.043028
222.885817	0.001088	222.975540	-0.089722	0.016804	0.037454
202.855603	0.000958	202.968233	-0.112630	0.017492	0.035483
182.825389	0.000829	182.923811	-0.098422	0.020629	0.037715
162.795175	0.000700	162.882719	-0.087544	0.026709	0.043481
150.777046	0.000622	150.888822	-0.111776	0.031956	0.048183
124.737768	0.000454	124.816460	-0.078693	0.048290	0.060236

Julie Marie Hovland, Ingeborg Lassen Bue

The uncertainty is calculated with 95% confidence. The uncertainty includes the randomness in the calibrated instrument during the calibration, systematic uncertainty in the instrument or property which the instrument under calibration is compared with (dead weight manometer, calibrated weights etc.), and due to regression analysis to fit the calibration points to a linear calibration equation. The calculated uncertainty can be used as the total systematic uncertainty of the calibrated instrument with the given calibration equation.

CALIBRATION REPORT

CALIBRATION PROPERTIES

Calibrated by: Julie Marie Hovland, Ingeborg Lassen Bue
Type/Producer: Kulite XTE-190
SN: v4537-34
Range: 0-7 bar a
Unit: kPa

CALIBRATION SOURCE PROPERTIES

Type/Producer: Pressurements deadweight tester P3223-1
SN: 66256
Uncertainty [%]: 0,01

POLY FIT EQUATION:

$Y = + 99.64090291E+0X^0 + 140.82223184E+3X^1$

CALIBRATION SUMMARY:

Max Uncertainty : 0.110693 [%]
Max Uncertainty : 0.110582 [kPa]
RSQ : 0.999998
Calibration points : 21

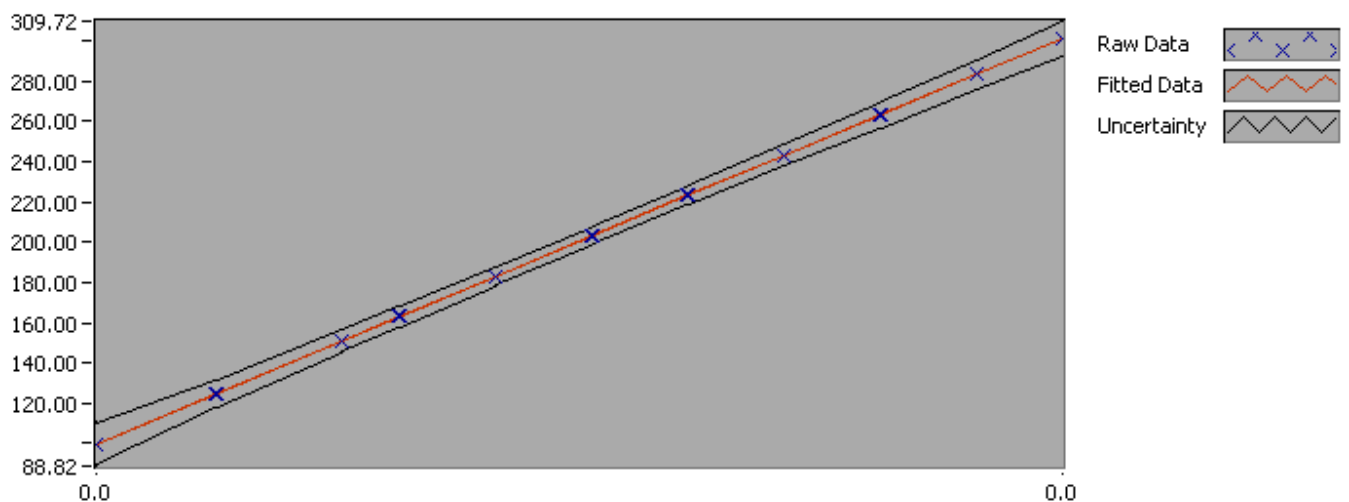


Figure 1 : Calibration chart (The uncertainty band is multiplied by 100)

Value [kPa]	Voltage [V]	Best Poly Fit [kPa]	Deviation [kPa]	Uncertainty [%]	Uncertainty [kPa]
99.900000	0.000002	99.877115	0.022885	0.110693	0.110582
124.937768	0.000179	124.815135	0.122633	0.055355	0.069160
150.977046	0.000364	150.861712	0.115334	0.036963	0.055805
162.995175	0.000449	162.909360	0.085815	0.031203	0.050860
183.025389	0.000591	182.928941	0.096448	0.024683	0.045176
203.055603	0.000734	202.983656	0.071947	0.021554	0.043766
223.085817	0.000876	223.012223	0.073595	0.021084	0.047036
243.116031	0.001018	243.043867	0.072165	0.022261	0.054121
263.146246	0.001161	263.070215	0.076031	0.024259	0.063836
283.176460	0.001303	283.093839	0.082621	0.026507	0.075062
301.203653	0.001431	301.116254	0.087399	0.028559	0.086021
283.176460	0.001303	283.187386	-0.010927	0.026507	0.075062
263.146246	0.001162	263.300350	-0.154104	0.024287	0.063911
243.116031	0.001020	243.235712	-0.119681	0.022311	0.054242
223.085817	0.000878	223.216102	-0.130284	0.021119	0.047112
203.055603	0.000735	203.185426	-0.129823	0.021557	0.043773
183.025389	0.000593	183.146597	-0.121208	0.024654	0.045122
162.995175	0.000450	163.074988	-0.079814	0.031169	0.050804
150.977046	0.000365	151.071941	-0.094895	0.036919	0.055740
124.937768	0.000180	124.956874	-0.019107	0.055286	0.069073
99.900000	0.000002	99.947030	-0.047030	0.097461	0.097363

Julie Marie Hovland, Ingeborg Lassen Bue

The uncertainty is calculated with 95% confidence. The uncertainty includes the randomness in the calibrated instrument during the calibration, systematic uncertainty in the instrument or property which the instrument under calibration is compared with (dead weight manometer, calibrated weights etc.), and due to regression analysis to fit the calibration points to a linear calibration equation. The calculated uncertainty can be used as the total systematic uncertainty of the calibrated instrument with the given calibration equation.

Calibration report

Calibration properties

Calibrated by: Sigrid Marie Skodje
 Type/producer: PTX 610
 SN: 2480173
 Range: 2.5bar a
 Unit: Bar

Calibrator properties

Type/producer: GE sensing Pressurements deadweight tester P3023-6-P
 SN: 66611
 Uncertainty: 0.008%

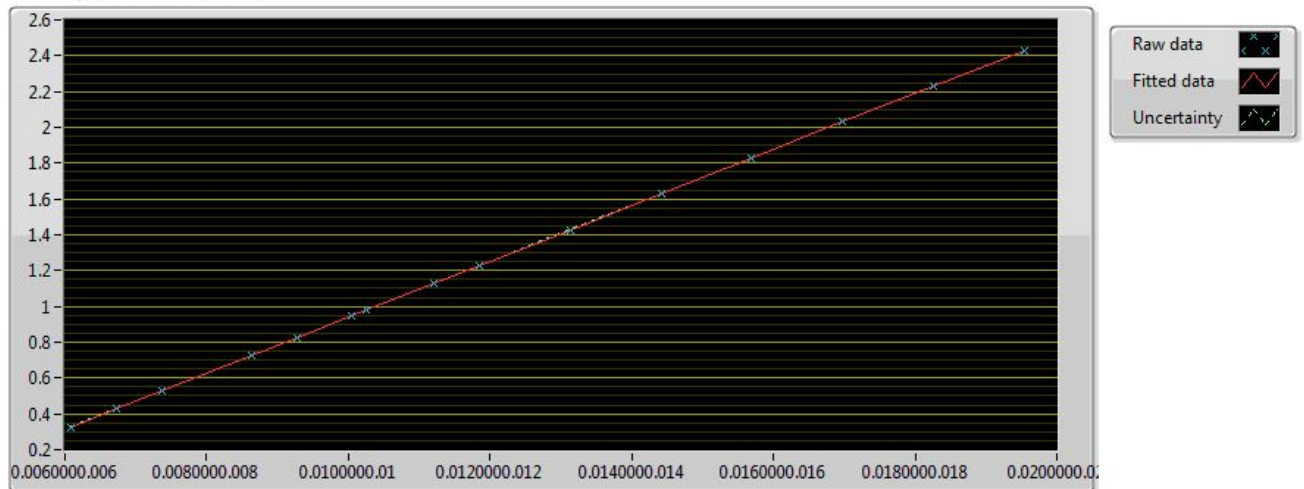
Calibration summary

Max Uncertainty: 0.000294[%]
 Max uncertainty: 0.056319[bar]
 Calibration points: 15.000000

Linear fit equation

$Y=156.167608x+-0.621796$

Raw data, best linear fit and errors



Logged calibration points

Pressure	Ampere	Best linear fit	Deviation	Uncertainty %	Uncertainty
0.327093	0.006078	0.327352	-0.000258	0.056319	0.000184
0.427244	0.006716	0.427060	0.000184	0.040400	0.000173
0.527396	0.007359	0.527433	-0.000037	0.030826	0.000163
0.727698	0.008640	0.727565	0.000133	0.020300	0.000148
0.827849	0.009284	0.828105	-0.000256	0.017257	0.000143
0.948030	0.010050	0.947660	0.000370	0.014669	0.000139
0.978075	0.010245	0.978185	-0.000110	0.014280	0.000140
1.128302	0.011206	1.128172	0.000130	0.012675	0.000143
1.228453	0.011850	1.228732	-0.000279	0.011900	0.000146
1.428755	0.013130	1.428618	0.000138	0.011152	0.000159
1.629057	0.014413	1.629005	0.000052	0.010974	0.000179
1.829359	0.015696	1.829429	-0.000070	0.011141	0.000204

2.029662	0.016978	2.029571	0.000090	0.011475	0.000233
2.229964	0.018260	2.229807	0.000157	0.011777	0.000263
2.430266	0.019545	2.430510	-0.000244	0.012104	0.000294

Dette er en footer

Calibration report

Calibration properties

Calibrated by: Sigrid Marie Skodje
Type/producer: PTX 610
SN: 2738456
Range: 2.5bar a
Unit: Bar

Calibrator properties

Type/producer: GE sensing Pressurements deadweight tester P3023-6-P
SN: 66611
Uncertainty: 0.008%

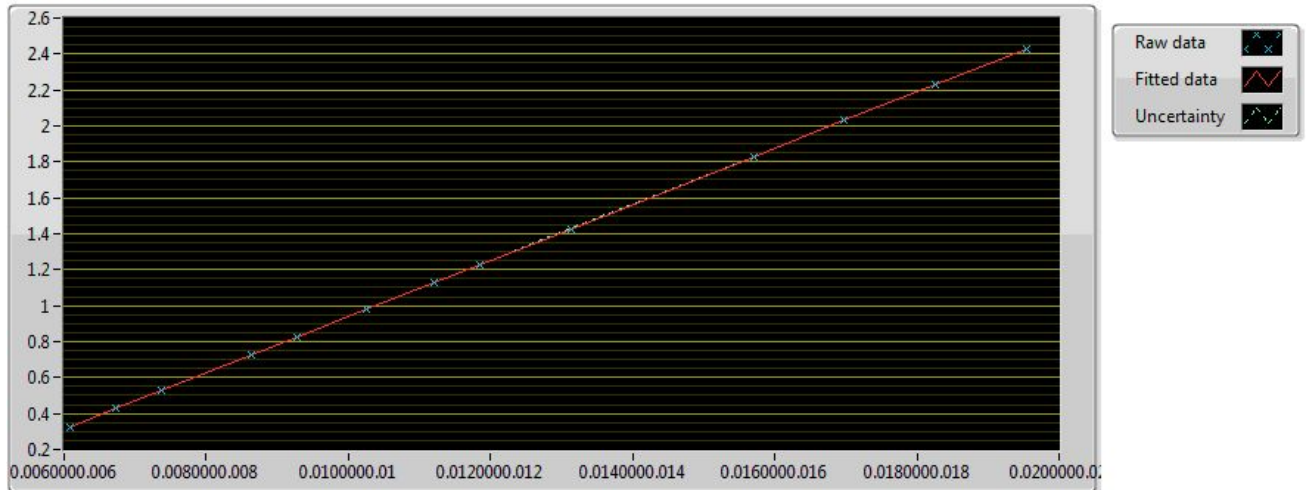
Calibration summary

Max Uncertainty: 0.000420[bar]
Max uncertainty: 0.094633[%]
Calibration points: 13

Linear fit equation

$Y=156.244957x-0.623428$

Raw data, best linear fit and errors



Logged calibration points

Pressure	Ampere	Best linear fit	Deviation	Uncertainty %	Uncertainty
0.326492	0.006077	0.326096	0.000397	0.094633	0.000309
0.426644	0.006719	0.426420	0.000224	0.067596	0.000288
0.526795	0.007361	0.526677	0.000118	0.051218	0.000270
0.727097	0.008644	0.727091	0.000006	0.032614	0.000237
0.827248	0.009284	0.827207	0.000041	0.027302	0.000226
0.977474	0.010246	0.977492	-0.000018	0.021701	0.000212
1.127701	0.011210	1.128112	-0.000411	0.018505	0.000209
1.227852	0.011851	1.228190	-0.000338	0.016956	0.000208
1.428154	0.013133	1.428566	-0.000412	0.015542	0.000222
1.828759	0.015697	1.829113	-0.000354	0.015582	0.000285
2.029061	0.016977	2.029192	-0.000131	0.016049	0.000326
2.229363	0.018257	2.229068	0.000295	0.016624	0.000371
2.429665	0.019537	2.429083	0.000582	0.017274	0.000420

Calibration report

Calibration properties

Calibrated by: Sigrid Marie Skodje
Type/producer: PTX 610
SN: 2738458
Range: 2.5bar a
Unit: Bar

Calibrator properties

Type/producer: GE sensing Pressurements deadweight tester P3023-6-P
SN: 66611
Uncertainty: 0.008%

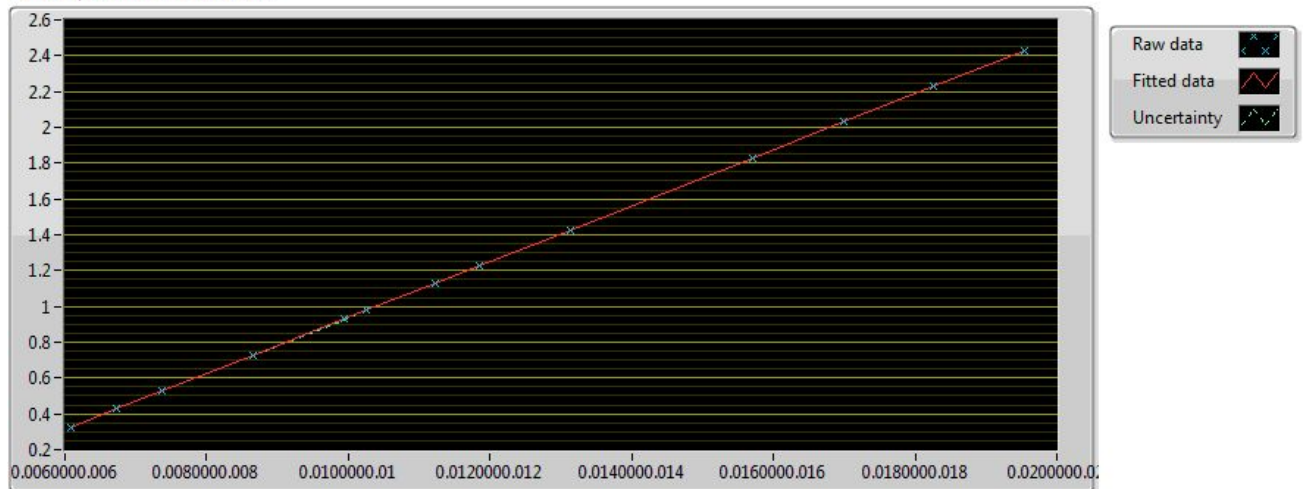
Calibration summary

Max Uncertainty: 0.000346[%]
Max uncertainty: 0.073927[bar]
Calibration points: 13.000000

Linear fit equation

$Y=156.237595x+-0.624527$

Raw data, best linear fit and errors



Logged calibration points

Pressure	Ampere	Best linear fit	Deviation	Uncertainty %	Uncertainty
0.326693	0.006087	0.326463	0.000230	0.073927	0.000242
0.426844	0.006729	0.426743	0.000101	0.052970	0.000226
0.526995	0.007369	0.526795	0.000200	0.040168	0.000212
0.727297	0.008653	0.727440	-0.000143	0.025996	0.000189
0.927599	0.009934	0.927552	0.000047	0.018743	0.000174
0.977675	0.010254	0.977602	0.000072	0.017550	0.000172
1.127901	0.011218	1.128182	-0.000281	0.015113	0.000170
1.228052	0.011859	1.228228	-0.000175	0.014198	0.000174
1.428355	0.013141	1.428513	-0.000158	0.013013	0.000186
1.828959	0.015706	1.829344	-0.000385	0.013003	0.000238
2.029261	0.016986	2.029357	-0.000096	0.013389	0.000272
2.229563	0.018267	2.229539	0.000025	0.013798	0.000308
2.429865	0.019546	2.429302	0.000564	0.014239	0.000346

Dette er en footer

CALIBRATION REPORT

CALIBRATION PROPERTIES

Calibrated by: Julie Marie Hovland og Ingeborg Lassen Bue
Type/Producer: Druck PTX 1400
SN: Y21674\07
Range: 0-10 bar g
Unit: kPa

CALIBRATION SOURCE PROPERTIES

Type/Producer: Pressurements deadweight tester P3223-1
SN: 66256
Uncertainty [%]: 0,01

POLY FIT EQUATION:

$Y = -147.56618266E+0X^0 + 124.99731727E+0X^1$

CALIBRATION SUMMARY:

Max Uncertainty : 0.067709 [%]
Max Uncertainty : 0.124951 [kPa]
RSQ : 1.000000
Calibration points : 12

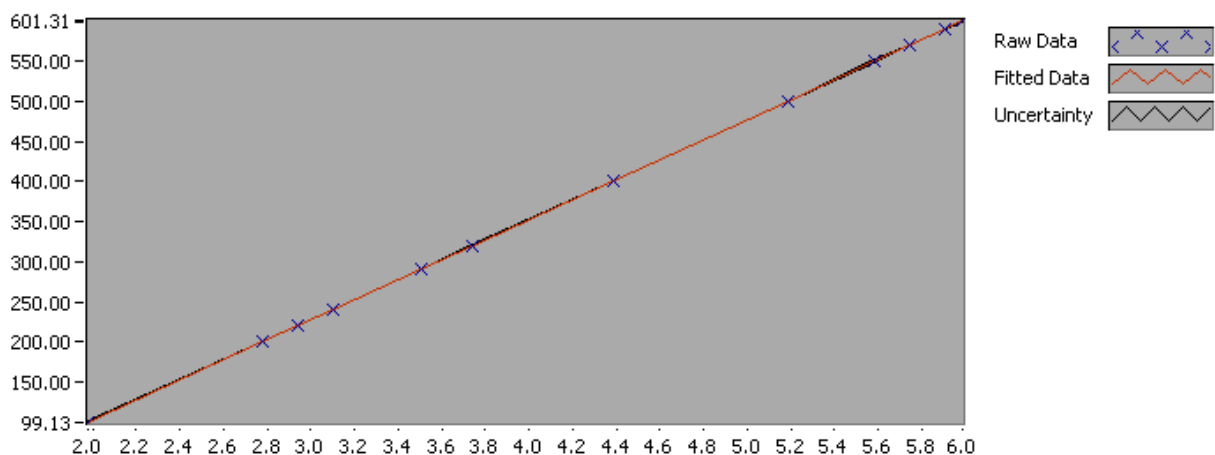


Figure 1 : Calibration chart (The uncertainty band is multiplied by 10)

Value [kPa]	Voltage [V]	Best Poly Fit [kPa]	Deviation [kPa]	Uncertainty [%]	Uncertainty [kPa]
99.918818	1.979021	99.806099	0.112719	0.067709	0.067654
200.069889	2.781602	200.126562	-0.056673	0.025646	0.051310
220.100104	2.941985	220.174045	-0.073941	0.022018	0.048462
240.130318	3.102203	240.200849	-0.070532	0.019079	0.045814
290.205853	3.502371	290.220771	-0.014918	0.013904	0.040350
320.251174	3.742425	320.226867	0.024308	0.011849	0.037945
400.372031	4.383175	400.318987	0.053044	0.009149	0.036632
500.523102	5.184437	500.474501	0.048601	0.008812	0.044104
550.598638	5.585022	550.546563	0.052075	0.022694	0.124951
570.628852	5.745752	570.637458	-0.008606	0.009480	0.054098
590.659066	5.906117	590.682590	-0.023524	0.009643	0.056959
600.674173	5.986392	600.716727	-0.042554	0.009856	0.059200

Julie Marie Hovland og Ingeborg Lassen Bue

COMMENTS: Lengst unna innløp

The uncertainty is calculated with 95% confidence. The uncertainty includes the randomness in the calibrated instrument during the calibration, systematic uncertainty in the instrument or property which the instrument under calibration is compared with (dead weight manometer, calibrated weights etc.), and due to regression analysis to fit the calibration points to a linear calibration equation. The calculated uncertainty can be used as the total systematic uncertainty of the calibrated instrument with the given calibration equation.

CALIBRATION REPORT

CALIBRATION PROPERTIES

Calibrated by: Julie Marie Hovland og Ingeborg Lassen Bue
Type/Producer: Druck PTX 1400
SN: Y21674\07
Range: 0-10 bar g
Unit: kPa

CALIBRATION SOURCE PROPERTIES

Type/Producer: Pressurements deadweight tester P3223-1
SN: 66256
Uncertainty [%]: 0,01

POLY FIT EQUATION:

$Y = -148.91611524E+0X^0 + 125.07688471E+0X^1$

CALIBRATION SUMMARY:

Max Uncertainty : 0.269190 [%]
Max Uncertainty : 0.268971 [kPa]
RSQ : 0.999998
Calibration points : 12

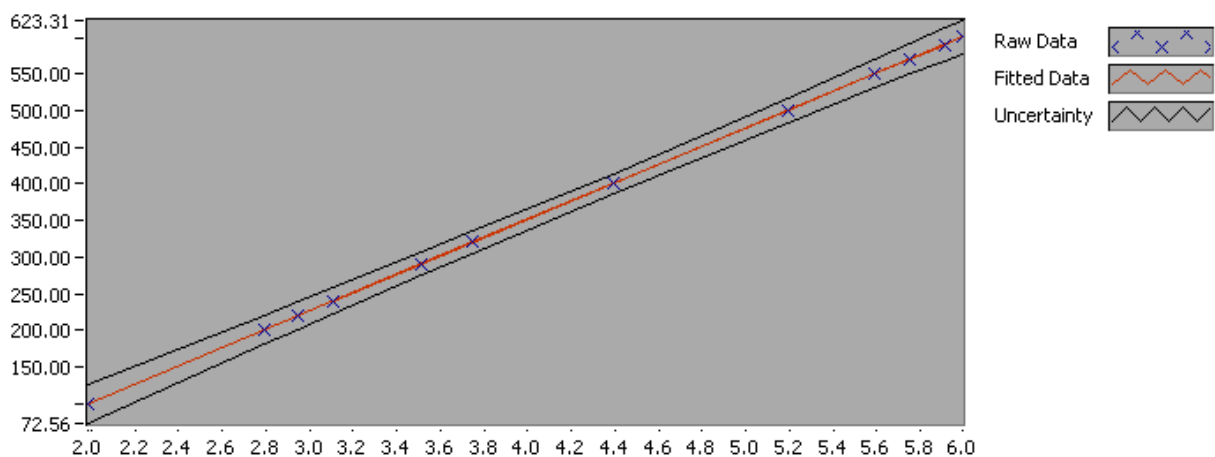


Figure 1 : Calibration chart (The uncertainty band is multiplied by 100)

Value [kPa]	Voltage [V]	Best Poly Fit [kPa]	Deviation [kPa]	Uncertainty [%]	Uncertainty [kPa]
99.918823	1.985731	99.452928	0.465895	0.269190	0.268971
200.069894	2.794882	200.659026	-0.589132	0.101223	0.202518
220.100108	2.949920	220.050696	0.049412	0.086881	0.191225
320.251179	3.750670	320.206061	0.045118	0.045921	0.147062
400.372036	4.391152	400.315549	0.056487	0.034741	0.139091
500.523107	5.191650	500.439245	0.083861	0.033768	0.169017
550.598642	5.592419	550.566235	0.032408	0.035499	0.195455
570.628856	5.752709	570.614863	0.013993	0.036338	0.207356
590.659071	5.913067	590.671831	-0.012761	0.037209	0.219776
600.674178	5.993021	600.672329	0.001849	0.037679	0.226329
290.205858	3.511148	290.247338	-0.041480	0.054134	0.157099
240.130322	3.111303	240.235972	-0.105650	0.075035	0.180182

Julie Marie Hovland og Ingeborg Lassen Bue

COMMENTS: Nærmest innløp

The uncertainty is calculated with 95% confidence. The uncertainty includes the randomness in the calibrated instrument during the calibration, systematic uncertainty in the instrument or property which the instrument under calibration is compared with (dead weight manometer, calibrated weights etc.), and due to regression analysis to fit the calibration points to a linear calibration equation. The calculated uncertainty can be used as the total systematic uncertainty of the calibrated instrument with the given calibration equation.



CALIBRATION REPORT

Parameter:	Pressure pulsations / dynamic pressure
Object identity:	Transducer VKL1740580 + amplifier VKL5015/1719297

Calibration equipment and settings:

Amplifier: VKL5015: 81.1pC/bar, 0.1bar/V, no filter, "Medium" mode ("Long" for calibration)
Oscilloscope: MR 8001: DC, 20ms/div, 0.5 -2V/div, trig level 1-0.3V, single seq. trig, noise rej.
DVM: MD 1007: DCV, resolution x.xxV, speed 3
Pressure reference: ME 110

Calibrated range:
100 kPa

Reference pressure [kPa]	Output [V]	Lin. est. [kPa]	Deviation	
			[kPa]	[%] OR
97.1	9.62	97.2	0.1	0.1
64.0	6.31	63.8	-0.2	-0.2
42.0	4.18	42.2	0.2	0.2
27.8	2.74	27.7	-0.1	-0.1
18.5	1.83	18.5	0.0	0.0

Calibration constants:

C_1 [kPa/V] C_0 [kPa] ¹⁾
10.10 0.0

1) $C_0=0$ in the data acq. program

Date / sign.: 2010-11-17 / *[Signature]*

CALIBRATION REPORT

CALIBRATION PROPERTIES

Calibrated by: Julie Marie Hovland og Ingeborg Lassen Bue

Type/Producer: Kraftcelle

SN:

Range:

Unit: Nm

CALIBRATION SOURCE PROPERTIES

Type/Producer: HBM 500kg load cell

SN: V4536-4

Uncertainty [%]: 0.01

POLY FIT EQUATION:

$Y = -197.79087116E+0X^0 + 488.34575988E+0X^1$

CALIBRATION SUMMARY:

Max Uncertainty : Inf [%]

Max Uncertainty : 1.299025 [Nm]

RSQ : 0.999990

Calibration points : 30

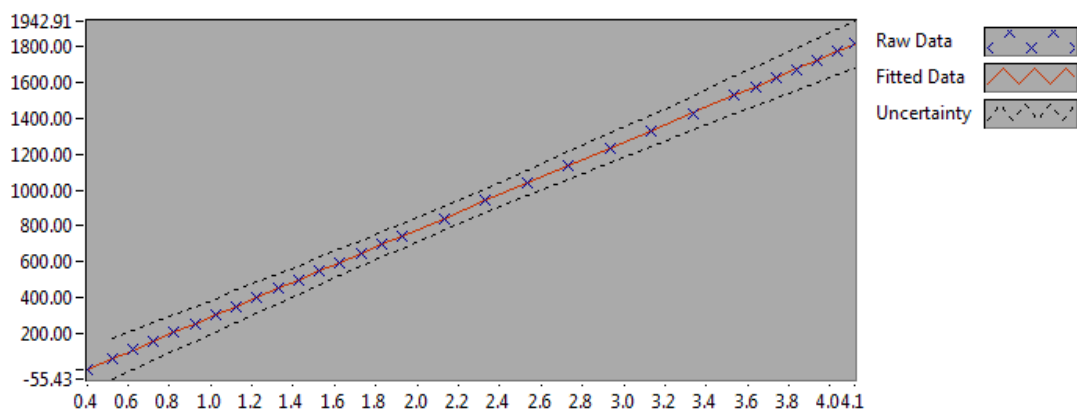


Figure 1 : Calibration chart (The uncertainty band is multiplied by 100)

Value [Nm]	Voltage [V]	Best Poly Fit [Nm]	Deviation [Nm]	Uncertainty [%]	Uncertainty [Nm]
0.000000	0.404404	-0.301804	0.301804	Inf	NaN
58.010483	0.522851	57.541113	0.469370	1.947428	1.129713
107.022337	0.623117	106.505601	0.516736	1.013938	1.085140
156.035171	0.723413	155.484843	0.550329	0.667682	1.041819
205.046241	0.823696	204.457504	0.588737	0.487570	0.999745
254.052802	0.924423	253.647147	0.405655	0.377573	0.959235
303.067695	1.025061	302.793189	0.274506	0.303285	0.919158
352.082391	1.125560	351.871776	0.210615	0.250254	0.881100
401.100519	1.226129	400.984031	0.116488	0.211135	0.846862
450.113353	1.326882	450.186165	-0.072812	0.181018	0.814788
499.131186	1.427474	499.309796	-0.178610	0.157401	0.785636
548.146961	1.528018	548.410131	-0.263171	0.138309	0.758136
597.159501	1.627829	597.152308	0.007193	0.122820	0.733430
646.169199	1.728898	646.508998	-0.339800	0.110509	0.714077
695.178602	1.829478	695.627105	-0.448503	0.100719	0.700177
744.188790	1.929540	744.491851	-0.303061	0.091843	0.683484
842.211028	2.130468	842.614251	-0.403224	0.080023	0.673963
940.195039	2.330855	940.472364	-0.277326	0.072708	0.683597
1038.199339	2.532208	1038.801939	-0.602600	0.068917	0.715495
1136.189722	2.733006	1136.861021	-0.671299	0.066332	0.753657
1234.180006	2.934665	1235.340580	-1.160574	0.065968	0.814159
1332.165781	3.133404	1332.393487	-0.227706	0.065892	0.877794
1430.148028	3.335123	1430.902311	-0.754283	0.066699	0.953891
1528.131353	3.536302	1529.147245	-1.015892	0.067967	1.038620
1577.124780	3.636754	1578.202528	-1.077749	0.068599	1.081898
1626.116442	3.737669	1627.483854	-1.367412	0.069290	1.126742
1675.117710	3.837849	1676.406539	-1.288829	0.069978	1.172220
1724.108392	3.938837	1725.723610	-1.615218	0.070571	1.216724
1773.100055	4.036806	1773.566097	-0.466042	0.071089	1.260487
1822.099069	4.117569	1813.006393	9.092676	0.071293	1.299025

Julie Marie Hovland og Ingeborg Lassen Bue

The uncertainty is calculated with 95% confidence. The uncertainty includes the randomness in the calibrated instrument during the calibration, systematic uncertainty in the instrument or property which the instrument under calibration is compared with (dead weight manometer, calibrated weights etc.), and due to regression analysis to fit the calibration points to a linear calibration equation. The calculated uncertainty can be used as the total systematic uncertainty of the calibrated instrument with the given calibration equation.

Appendix B - Defect blade sensors

During calibration of the runner transducers it was discovered that water was leaking out from the insulation sockets. It was also apparent that several transducers had experienced water penetration and was no longer working. The calibration tank was then pressurized to 2 barg and left overnight. The next day a total of 9 transducers were still working after completing the calibration.

It was first assumed that water penetrated into the joint from the extension of the wires. However, when the tank was opened it was discovered that only two of the damaged transducers were extended. It was also discovered that not all of the transducers that had water through its socket were damaged.

It is thought that the main problem with these transducers is the teflon socket that is thread over the transducer wires. The epoxy that is filled into the milled groove on the blade does not seem to stick well to the teflon socket, hence water is able to penetrate into the sensor between the socket and the epoxy.

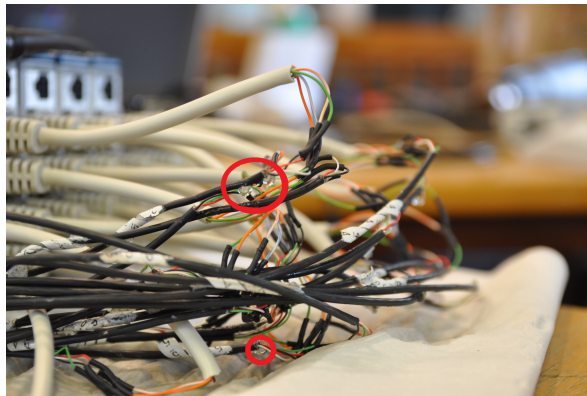


Figure 8.1: Water leaking out of transducers

Appendix C - Rig setup

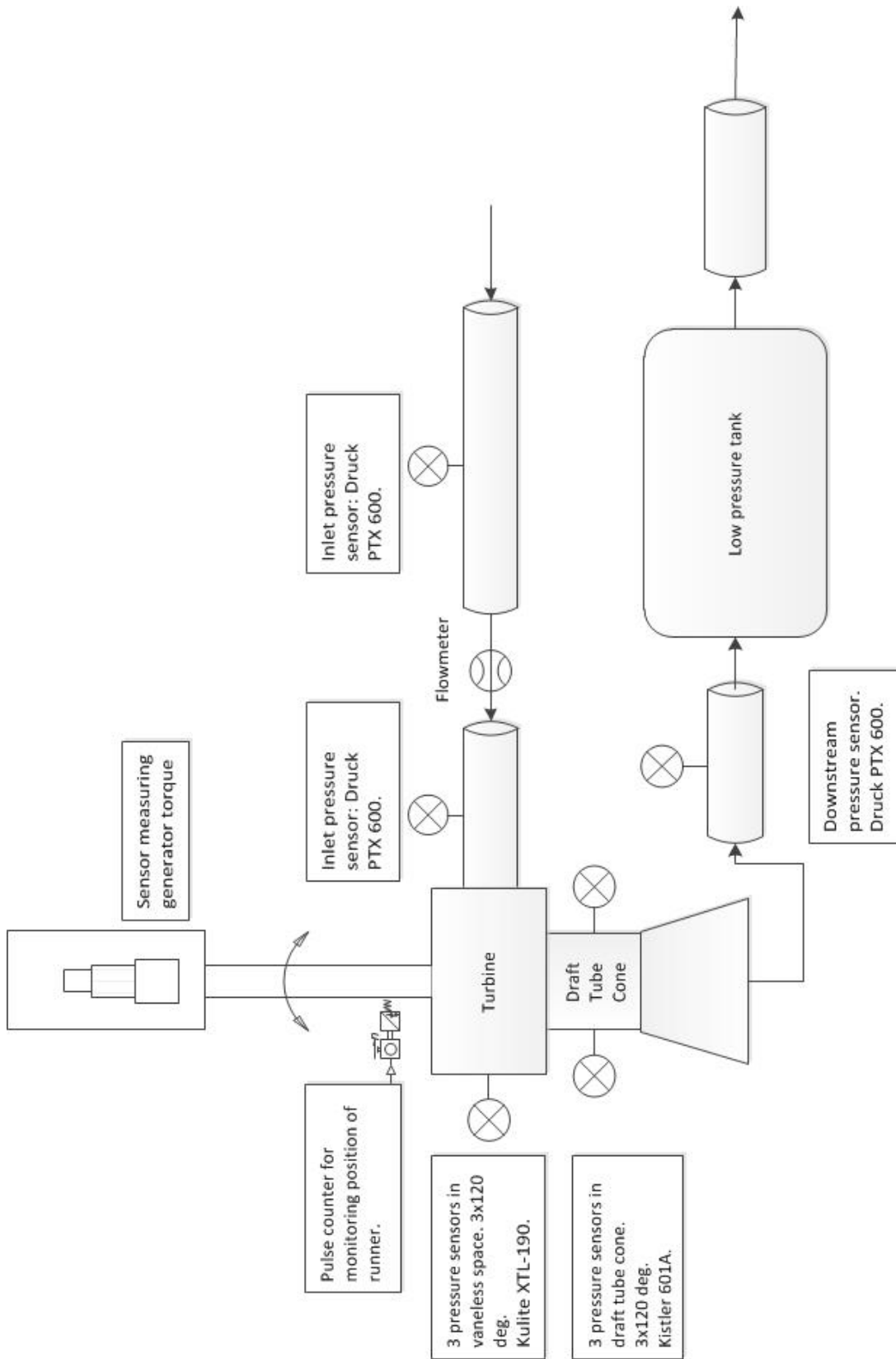


Figure 8.2: Setup of Francis rig with sensors in stationary frame

Appendix D - Air leakage

An air leakage caused excessive swirls in the draft tube. The opening in the shaft was filled with epoxy in an attempt to stop the leakage (See Figure 8.3).

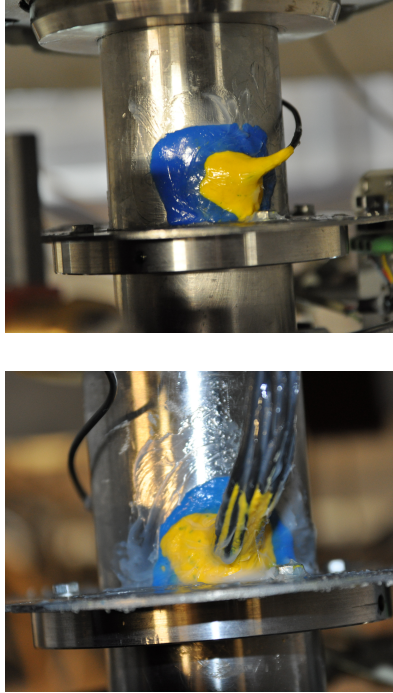


Figure 8.3: Wire opening filled with epoxy

Appendix E - Compact RIO Installation

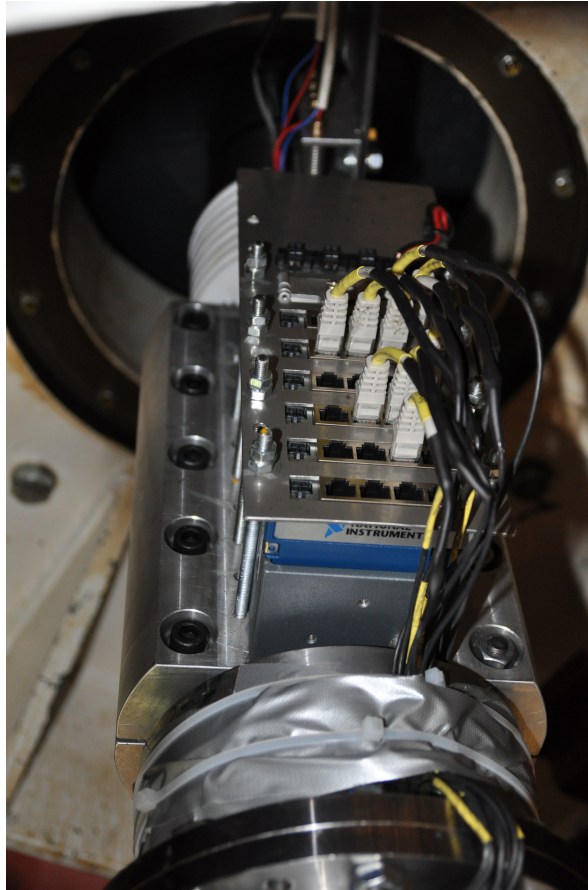


Figure 8.4: Compact RIO mounted on shaft

Appendix F - Results

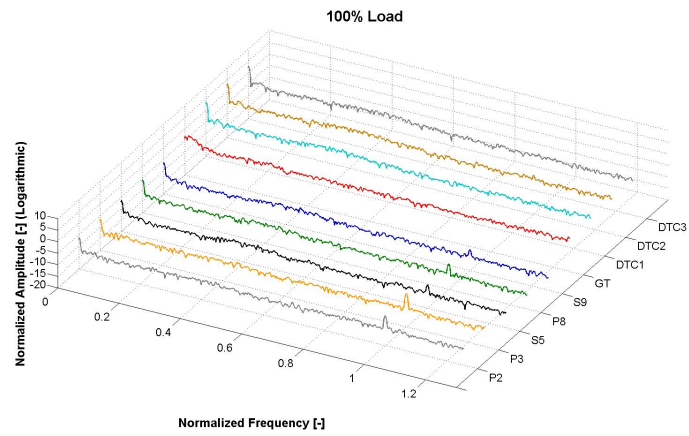


Figure 8.5: Lower frequency domain at 100% load

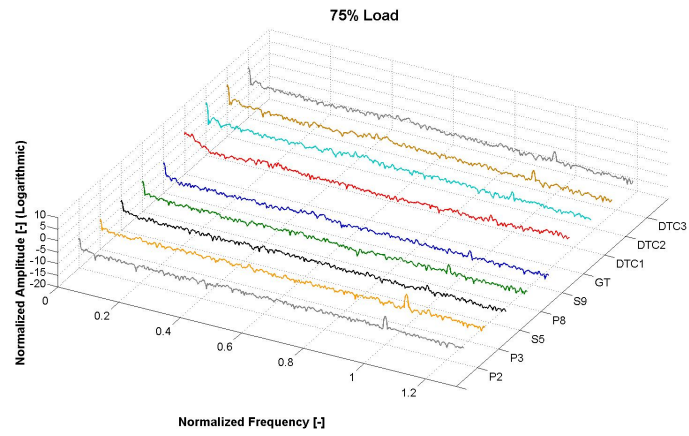


Figure 8.6: Lower frequency domain at 75% load

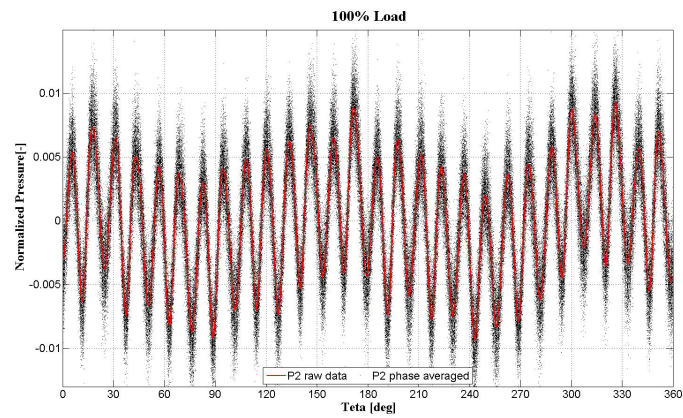


Figure 8.7: Phase averaging of runner sensor P2 at 100% load

Appendix G - Risk assesment

Risikovurderingsrapport

Francisriggen

Prosjekttittel	Modelltest
Prosjektleder	Torbjørn K. Nielsen
Enhet	NTNU
HMS-koordinator	Erik Langørgen
Linjeleder	Olav Bolland
Plassering	Vannkraftlaboratoriet
Romnummer	42
Riggansvarlig	Ingeborg L. Bue og Julie M. Hovland
Risikovurdering utført av	Ingeborg L. Bue og Julie M. Hovland

TABLE OF CONTENTS

1	INTRODUCTION	1
2	ORGANISATION	1
3	RISK MANAGEMENT IN THE PROJECT	1
4	DRAWINGS, PHOTOS, DESCRIPTIONS OF TEST SETUP	1
5	EVACUATION FROM THE EXPERIMENT AREA	1
6	WARNING	2
6.1	Before experiments.....	2
6.2	Nonconformance.....	2
7	ASSESSMENT OF TECHNICAL SAFETY	3
7.1	HAZOP.....	3
7.2	Flammable, reactive and pressurized substances and gas	3
7.3	Pressurized equipment.....	3
7.4	Effects on the environment (emissions, noise, temperature, vibration, smell)	3
7.5	Radiation	3
7.6	Usage and handling of chemicals.....	3
7.7	El safety (need to deviate from the current regulations and standards.)	4
8	ASSESSMENT OF OPERATIONAL SAFETY	4
8.1	Prosedure HAZOP	4
8.2	Operation and emergency shutdown procedure.....	4
8.3	Training of operators.....	4
8.4	Technical modifications.....	4
8.5	Personal protective equipment.....	4
	8.5.1 General Safety	5
8.6	Safety equipment	5
8.7	Special actions.....	5
9	QUANTIFYING OF RISK - RISK MATRIX.....	5
10	CONCLUSJON	5
11	REGULATIONS AND GUIDELINES	6
12	DOCUMENTATION.....	7
13	GUIDANCE TO RISK ASSESSMENT TEMPLATE	7

1 INTRODUCTION

Description of experiment setup and the purpose of the experiments. Where is the rig located?

2 ORGANISATION

Rolle	NTNU	Sintef
Lab Ansvarlig:	Morten Grønli	Harald Mæhlum
Linjeleder:	Olav Bolland	Mona Mølsvik
HMS ansvarlig:	Olav Bolland	Mona Mølsvik
HMS koordinator	Erik Langørgen	Harald Mæhlum
HMS koordinator	Bård Brandåstrø	
Romansvarlig:	Bård Brandåstrø	
Prosjekt leder:	Torbjørn Nielsen	
Ansvarlig riggoperatører:	Ingeborg L. Bue og Julie M. Hovland	

3 RISK MANAGEMENT IN THE PROJECT

Hovedaktiviteter risikostyring	Nødvendige tiltak, dokumentasjon	DATE
Prosjekt initiering	Prosjekt initiering mal	
Veiledningsmøte Guidance Meeting	Skjema for Veiledningsmøte med pre-risikovurdering	
Innledende risikovurdering Initial Assessment	Fareidentifikasjon – HAZID Skjema grovanalyse	
Vurdering av teknisk sikkerhet Evaluation of technical security	Prosess-HAZOP Tekniske dokumentasjoner	
Vurdering av operasjonell sikkerhet Evaluation of operational safety	Prosedyre-HAZOP Opplæringsplan for operatører	
Sluttvurdering, kvalitetssikring Final assessment, quality assurance	Uavhengig kontroll Utstedelse av apparaturkort Utstedelse av forsøk pågår kort	

4 DRAWINGS, PHOTOS, DESCRIPTIONS OF TEST SETUP

Attachments:

Process and Instrumentation Diagram (PID)

Shall contain all components in the experimental setup

Component List with specifications

Drawings and photos describing the setup.

Where the operator is present, how is the gas bottles, shutdown valves for water / air.

5 EVACUATION FROM THE EXPERIMENT AREA

Evacuate at signal from the alarm system or local gas alarms with its own local alert with sound and light outside the room in question, see 6.2

Evacuation from the rigging area takes place through the marked emergency exits to

the assembly point, (corner of Old Chemistry Kjelhuset or parking 1a-b.)

Action on rig before evacuation:

(Shut off the air and water supply. Power off the electrical supply.)

6 WARNING

6.1 Before experiments

E-mail with information about the planned experiment to: iept-experiments@ivt.ntnu.no

The e-mail should contain the following items:

- Name of responsible person:
- Experimental setup/rig:
- Start Experiments: (date and time)
- Stop Experiments: (date and time)

You should get the approval back from the laboratory management before start up. All running experiments are notified in the activity calendar for the lab to be sure they are coordinated with other activity.

6.2 Nonconformance

FIRE

Fire you are not able to put out with locally available fire extinguishers, activate, the nearest fire alarm and evacuate area. Be then available for fire brigade and building caretaker to detect fire place.

If possible, notify:

NTNU	SINTEF
Labsjef Morten Grønli, tlf: 918 97 515	Labsjef Harald Mæhlum, : tlf 930 149 86
HMS: Morten Grønli, tlf: 918 97 515 HMS: Per Bjørnaas, tlf: 91897123	Forskningsjef Mona Mølsvik
Instituttleder: Olav Bolland: 91897209	
NTNU Sintef Beredskapstelefon	800 80 388

GASALARM

At a gas alarm, close gas bottles immediately and ventilated the area. If the level of gas concentration not decrease within a reasonable time, activate the fire alarm and evacuate the lab. Designated personnel or fire department checks the leak to determine whether it is possible to seal the leak and ventilate the area in a responsible manner.

Alert Order in the above paragraph.

PERSONAL INJURY

- First aid kit in the fire / first aid stations
- , Shout for help
- Start life-saving first aid•

CALL 113 if there is any doubt whether there is a serious injury

Other Nonconformance (AVVIK)

NTNU:

Reporting nonconformance, Innsida, avviksmelding:

https://innsida.ntnu.no/lenkesamling_vis.php?katid=1398

SINTEF:

Synergi

7 ASSESSMENT OF TECHNICAL SAFETY

7.1 HAZOP

See Chapter 13 "Guide to the report template".

The experiment set up is divided into the following nodes:

Node 1	Pipe system with pump
Node 2	Rotating turbine/shaft with mounted hardware
Node 3	Hydraulics

Attachments:, skjema: Hazop

Conclusion:

Vurdering:

Node1:

- Overtrykksventil som slår ut dersom trykket i systemet blir for høyt.
- Rørelementer er eksternt levert og godkjent for aktuelt trykk.

Node2:

- Roterende utstyr står utilgjengelig for folk. Dvs det er innkapslet eller man må klatre for å nå opp til det.

Node3:

- Trykk i slanger og rør(olje vann) Hydraulikkslanger er ikke egenprodusert, men trykksatt
- Trykksatt utstyr er sertifisert og kjøpt inn av eksterne leverandører med god kompetanse

7.2 Flammable, reactive and pressurized substances and gas

Contains the experiments Flammable, reactive and pressurized substances and gas

JA	Trykksatt hydraulikkolje, trykksatt vann
----	--

Attachments:

Conclusion: Arbeidsmedium er vann. Alle rør er levert av eksternt firma med prøvesertifikat Hydraulikk til hydrostatisk lager. Hyllevarer komponenter, de er dermed ikke egenprodusert.

7.3 Pressurized equipment

Contain the set up pressurized equipment?

JA	Utstyret trykktestes i henhold til norm og dokumenteres
----	---

Attachments:

Conclusion: Prøvesertifikat for trykktesting finnes i labperm.

7.4 Effects on the environment (emissions, noise, temperature, vibration, smell)

NEI	
-----	--

Conclusion:

7.5 Radiation

See Chapter 13 "Guide to the report template".

NEI	
-----	--

Attachments:

Conclusion:

7.6 Usage and handling of chemicals.

See Chapter 13 "Guide to the report template".

JA	
----	--

Attachments: MSDS

Conclusion: Hydraulikkolje, mineralsk olje. Datablad er vedlagt.

7.7 El safety (need to deviate from the current regulations and standards.)

NEI	
-----	--

Attachments:

Conclusion: Alt elektrisk utstyr er forsvarlig montert og står slik permanent.

8 ASSESSMENT OF OPERATIONAL SAFETY

For ensuring that established procedures cover all identified risk factors that must be taken care of through procedures and ensure that the operators and technical performance have sufficient expertise.

8.1 Prosedure HAZOP

See Chapter 13 "Guide to the report template".

The method is a procedure to identify causes and sources of danger to operational problems.

Attachments: HAZOP_MAL_Proseedyre

Conclusion: Operatør har et eget rom for å kjøre riggen.

8.2 Operation and emergency shutdown procedure

See Chapter 13 "Guide to the report template".

The operating procedure is a checklist that must be filled out for each experiment.

Emergency procedure should attempt to set the experiment set up in a harmless state by unforeseen events.

Attachments: Procedure for running experiments

Emergency shutdown procedure: Nødstopp i kontrollrom.

8.3 Training of operators

A Document showing training plan for operators

- Kjøring av pumpesystem.

Vedlegg: Opplæringsplan for operatører

8.4 Technical modifications

- Technical modifications made by the Operator
 - o None
- • Technical modifications that must be made by Technical staff:
 - o Everything
- • What technical modifications give a need for a new risk assessment; (by changing the risk picture)?

Conclusion: Modifikasjoner gjøres i samråd med Torbjørn Nielsen/Bård Brandåstrø

8.5 Personal protective equipment

- It is mandatory use of eye protection in the rig zone

Conclusion: Vernebriller viktig, pga vann og hydraulikkolje under trykk.

8.5.1 General Safety

Conclusion: Alle forsøk kjøres med operatør til stede og en fast ansatt tilgjengelig på vannkraftlaboratoriet.

8.6 Safety equipment

- Vernebriller

8.7 Special actions

9 QUANTIFYING OF RISK - RISK MATRIX

See Chapter 13 "Guide to the report template".

The risk matrix will provide visualization and an overview of activity risks so that management and users get the most complete picture of risk factors.

IDnr	Aktivitet-hendelse	Frekv-Sans	Kons	RV
1	Lekkasje i Hydraulikk	1	A	A1
2	Fremmedlegemer i vannet	1	A	A1
3	Rørbrudd	1	A	A1
4	Roterende Aksling	1	B	B1
5	Roterende festebrakett med hardware	1	A	A1

Conclusion : *Det er liten restrisiko ved forsøkene, foruten at trykksatt vann og olje fordrer bruk av vernebriller. Fremmedlegemer i vannet gir liten risiko for personskade, men kan føre til store skader på maskineri.*

10 CONCLUSJON

Riggen er bygget til god laboratorium praksis (GLP).

Hvilke tekniske endringer av driftsparametere vil kreve ny risikovurdering:

Komponent mot komponent krever ikke. Ellers må ny risikovurdering utføres.

Apparaturkortet får en gyldighet på **4 måneder**.

Forsøk pågår kort får en gyldighet på **4 måneder**.

11 REGULATIONS AND GUIDELINES

Se <http://www.arbeidstilsynet.no/regelverk/index.html>

- Lov om tilsyn med elektriske anlegg og elektrisk utstyr (1929)
- Arbeidsmiljøloven
- Forskrift om systematisk helse-, miljø- og sikkerhetsarbeid (HMS Internkontrollforskrift)
- Forskrift om sikkerhet ved arbeid og drift av elektriske anlegg (FSE 2006)
- Forskrift om elektriske forsyningsanlegg (FEF 2006)
- Forskrift om utstyr og sikkerhetssystem til bruk i eksplosjonsfarlig område NEK 420
- Forskrift om håndtering av brannfarlig, reaksjonsfarlig og trykksatt stoff samt utstyr og anlegg som benyttes ved håndteringen
- Forskrift om Håndtering av eksplosjonsfarlig stoff
- Forskrift om bruk av arbeidsutstyr.
- Forskrift om Arbeidsplasser og arbeidslokaler
- Forskrift om Bruk av personlig verneutstyr på arbeidsplassen
- Forskrift om Helse og sikkerhet i eksplosjonsfarlige atmosfærer
- Forskrift om Høytrykksspyling
- Forskrift om Maskiner
- Forskrift om Sikkerhetsskilting og signalgivning på arbeidsplassen
- Forskrift om Stillaser, stiger og arbeid på tak m.m.
- Forskrift om Sveising, termisk skjæring, termisk sprøyting, kullbuemeisling, lodding og sliping (varmt arbeid)
- Forskrift om Tekniske innretninger
- Forskrift om Tungt og ensformig arbeid
- Forskrift om Vern mot eksponering for kjemikalier på arbeidsplassen (Kjemikalieforskriften)
- Forskrift om Vern mot kunstig optisk stråling på arbeidsplassen
- Forskrift om Vern mot mekaniske vibrasjoner
- Forskrift om Vern mot støy på arbeidsplassen

Veiledninger fra arbeidstilsynet

se: <http://www.arbeidstilsynet.no/regelverk/veiledninger.html>

12 DOCUMENTATION

- Tegninger, foto, beskrivelser av forsøksoppsetningen
- Hazop_mal
- Sertifikat for trykkpåkjent utstyr
- Håndtering avfall i NTNU
- Sikker bruk av LASERE, retningslinje
- HAZOP_MAL_Prosedyre
- Forsøksprosedyre
- Opplæringsplan for operatører
- Skjema for sikker jobb analyse, (SJA)
- Apparatorkortet
- Forsøk pågår kort

13 GUIDANCE TO RISK ASSESSMENT TEMPLATE

Kap 7 Assessment of technical safety.

Ensure that the design of the experiment set up is optimized in terms of technical safety.

Identifying risk factors related to the selected design, and possibly to initiate re-design to ensure that risk is eliminated as much as possible through technical security.

This should describe what the experimental setup actually are able to manage and acceptance for emission.

7.1 HAZOP

The experimental set up is divided into nodes (eg motor unit, pump unit, cooling unit.). By using guidewords to identify causes, consequences and safeguards, recommendations and conclusions are made according to if necessary safety is obtained. When actions are performed the HAZOP is completed.

(e.g. "No flow", cause: the pipe is deformed, consequence: pump runs hot, precaution: measurement of flow with a link to the emergency or if the consequence is not critical used manual monitoring and are written into the operational procedure.)

7.2 Flammable, reactive and pressurized substances and gas.

According to the Regulations for handling of flammable, reactive and pressurized substances and equipment and facilities used for this:

<p>Flammable material: Solid, liquid or gaseous substance, preparation, and substance with occurrence or combination of these conditions, by its flash point, contact with other substances, pressure, temperature or other chemical properties represent a danger of fire.</p>
--

<p>Reactive substances: Solid, liquid, or gaseous substances, preparations and substances that occur in combinations of these conditions, which on contact with water, by its pressure, temperature or chemical conditions, represents a potentially dangerous reaction, explosion or release of hazardous gas, steam, dust or fog.</p>
--

<p>Pressurized : Other solid, liquid or gaseous substance or mixes having fire or hazardous material response, when under pressure, and thus may represent a risk of uncontrolled emissions</p>
--

Further criteria for the classification of flammable, reactive and pressurized substances are set out in Annex 1 of the Guide to the Regulations "Flammable, reactive and pressurized substances"

<http://www.dsb.no/Global/Publikasjoner/2009/Veiledning/Generell%20veiledning.pdf>

http://www.dsb.no/Global/Publikasjoner/2010/Tema/Temaveiledning_bruk_av_farlig_stoff_Del_1.pdf

Experiment setup area should be reviewed with respect to the assessment of Ex zone

- Zone 0: Always explosive atmosphere, such as inside the tank with gas, flammable liquid.
- Zone 1: Primary zone, sometimes explosive atmosphere such as a complete drain point
- Zone 2: secondary discharge could cause an explosive atmosphere by accident, such as flanges, valves and connection points

7.4 Effects on the environment

With pollution means: bringing solids, liquid or gas to air, water or ground, noise and vibrations, influence of temperature that may cause damage or inconvenience effect to the environment.

Regulations: <http://www.lovdatabasen.no/all/hl-19810313-006.html#6>

NTNU guidance to handling of waste: <http://www.ntnu.no/hms/retningslinjer/HMSR18B.pdf>

7.5 Radiation

Definition of radiation

Ionizing radiation: Electromagnetic radiation (in radiation issues with wavelength <100 nm) or rapid atomic particles (e.g. alpha and beta particles) with the ability to stream ionized atoms or molecules.

Non ionizing radiation: Electromagnetic radiation (wavelength >100 nm), og ultrasound₁ with small or no capability to ionize.

Radiation sources: All ionizing and powerful non-ionizing radiation sources.

Ionizing radiation sources: Sources giving ionizing radiation e.g. all types of radiation sources, x-ray, and electron microscopes.

Powerful non ionizing radiation sources: Sources giving powerful non ionizing radiation which can harm health and/or environment, e.g. class 3B and 4. MR₂ systems, UVC₃ sources, powerful IR sources₄.

₁Ultrasound is an acoustic radiation ("sound") over the audible frequency range (> 20 kHz). In radiation protection regulations are referred to ultrasound with electromagnetic non-ionizing radiation.

₂MR (e.g. NMR) - nuclear magnetic resonance method that is used to "depict" inner structures of different materials.

₃UVC is electromagnetic radiation in the wavelength range 100-280 nm.

₄IR is electromagnetic radiation in the wavelength range 700 nm - 1 mm.

For each laser there should be an information binder (HMSRV3404B) which shall include:

- General information
- Name of the instrument manager, deputy, and local radiation protection coordinator
- Key data on the apparatus
- Instrument-specific documentation
- References to (or copies of) data sheets, radiation protection regulations, etc.
- Assessments of risk factors
- Instructions for users